Adaptor protein supersaturation drives innate immune signaling and cell fate

Alejandro Rodriguez Gama[1], Tayla Miller[1], Shriram Venkatesan[1], Jeffrey J. Lange[1], Jianzheng Wu[1], Xiaoqing Song[1], William D. Bradford[1], Malcolm Cook[1], Jay R. Unruh[1], Randal Halfmann[1,2]

1. Stowers Institute for Medical Research, Kansas City, MO, USA.
2. Department of Biochemistry and Molecular Biology, University of Kansas Medical Center, Kansas City, KS, USA

Summary

How minute pathogenic signals trigger decisive immune responses is a fundamental question in biology. Classical signaling often relies on ATP-driven enzymatic cascades, but innate immunity frequently employs death fold domain (DFD) self-assembly. The energetic basis of this assembly is unknown. Here, we show that specific DFDs function as energy reservoirs through metastable supersaturation. Characterizing all 109 human DFDs, we identified sequence-encoded nucleation barriers specifically in the central adaptors of inflammatory signalosomes, allowing them to accumulate far above their saturation concentration while remaining soluble and poised for activation. We demonstrate that the inflammasome adaptor ASC is constitutively supersaturated *in vivo*, retaining energy that powers on-demand cell death. Swapping a non-supersaturable DFD in the apoptosome with a supersaturable one sensitized cells to sublethal stimuli. Mapping all DFD nucleating interactions revealed that supersaturated adaptors are triggered to polymerize specifically by other DFDs in their respective pathways, limiting potentially deleterious crosstalk. Across human cell types, adaptor supersaturation strongly correlates with cell turnover, implicating this thermodynamic principle in the trade-off between immunity and longevity. Profiling homologues from fish and sponge, we find nucleation barriers to be conserved across metazoa. These findings reveal DFD adaptors as biological phase change materials in thermal batteries to power cellular life-or-death decisions on demand.

Main

Innate immune signaling transduces small signals to robust responses such as programmed cell death and/or inflammation. Signaling occurs when danger- or pathogen-associated molecular patterns (D/PAMPs) activate cognate receptor proteins that then activate effector proteins such as caspases, typically via one or more intermediary proteins known as adaptors.

While the binding of a D/PAMP to receptors initiates signaling, this initial interaction releases insufficient energy to directly change cell state. That tiny signal must be amplified in an energy consuming process that is fundamental to understanding the architecture and evolution of these critical signaling networks.[1–3] Innate immune signaling networks from bacteria to humans amplify signaling through interactions between nonenzymatic death fold domains (DFDs), which comprise the caspase recruitment domain (CARD), death domain (DD), death effector domain (DED), and pyrin domain (PYD) subfamilies.[4–8] However, the energetic basis for DFD function has been the subject of considerable speculation but remains largely unresolved (**Figure 1A**).

DFDs commonly form paracrystalline polymers that can template their own growth when free subunits exceed their saturation concentration (C_{sat}). Polymers are functionally initiated by D/PAMP-bound receptor oligomerization. To preclude signaling through spontaneous nucleation, DFDs are presumed to be effectively subsaturated prior to activation, through a combination of low basal expression, subcellular compartmentalization, post-translational modifications, and regulatory interactions.[4,9–11] We previously discovered, however, that the DFD-containing adaptor Bcl10 exhibits an intrinsic (sequence-encoded) nucleation barrier that is large enough to support persistent deep supersaturation in vivo, allowing it to amplify signaling independently of orthogonal input.[12]

The increased ordering of DFD subunits in polymers relative to those in solution implies that polymerization releases heat. Here, we propose that DFD-containing signalosomes broadly function as a form of thermal battery -- an on-demand energy reservoir that can be discharged via latent heat release through a specific external input.[13] Energy storage is accomplished via metastable supersaturation by a phase change material. A familiar example of a phase change material is the sodium acetate solution inside reusable hand warmers, which releases heat when the metal disk inside is pressed to nucleate crystalline sodium acetate trihydrate. Supersaturation is a state where a solute's concentration exceeds C_{sat} yet remains in solution due to a structurally-determined nucleation barrier. In the context of innate immune signalosomes, at least one DFD would function as the phase change material by constitutively exceeding its C_{sat}, allowing the signalosome to assemble immediately upon D/PAMP-triggered nucleation. Although heat will necessarily be released during the phase transition, it dissipates far too quickly to influence downstream signaling.[14] This mechanism would allow cells to respond to D/PAMPs decisively and independently of metabolism, which is frequently compromised during infection.[15] For DFDs to function in this manner, their endogenous concentration would need to greatly exceed their respective C_{sat} values, while they nevertheless remain soluble over timescales spanning the

window of vulnerability to infection, i.e. the full lifetimes of cells. Cells would therefore be continuously susceptible to spontaneous death and inflammation through stochastic nucleation events, imposing a fundamental tradeoff between immunity and longevity.

We here use a combination of biophysical, bioinformatic, and cytological approaches to investigate the capacity and functional relevance of supersaturation by human DFDs. Our results collectively uncover the energetic basis for signal amplification by DFDs and in turn a thermodynamic drive to die.

A select subset of DFDs have intrinsic nucleation barriers enabling persistent supersaturation

To systematically survey the ability of DFDs to supersaturate, we compiled an exhaustive set of 109 structurally independent human DFDs (**Table S1 and Figure S1A-B**) and then characterized their tendency to spontaneously self-assemble in near-physiological conditions while minimizing interference from other proteins. For this purpose we used distributed amphifluoric FRET (DAmFRET) in an orthogonal eukaryotic host that completely lacks endogenous DFDs and their associated regulatory machinery -- *Saccharomyces cerevisiae*. DAmFRET produces a snapshot of the population-level distribution of single-cell measurements of ratiometric FRET ("AmFRET") between two fluorescent forms of the same protein species.[16] The data revealed a diversity of behaviours (**Figure 1B-C, S1C-D, and Table S1**), ranging from no self-association to self-association in all cells at all concentrations. Importantly, the results closely agree with observations of individual DFDs in the literature. Considering the adaptor FADD as an example, its DD was monomeric whereas its DED assembled robustly, consistent with prior observations that the DD forms exclusively hetero-oligomers while the DED forms homopolymers.[17–19] Twenty-one DFDs transitioned from no to high AmFRET in a discontinuous manner, the signature of a large intrinsic nucleation barrier.[12,16,20]

Nucleation barriers increase with the entropic cost of assembly.[16,21] Consequently, assemblies with large barriers tend to be more ordered than those without. Ordered assembly by DFDs occurs as a two-dimensional array twisted into a one-dimensional polymer[22–24] that can manifest as microscopically visible filaments in cells.[12,23,25] To evaluate the expected relationship between nucleation barriers and ordered assembly, we used high-throughput confocal microscopy to examine the subcellular distribution of each protein. We observed subcellular assemblies for most of the DFDs that populated AmFRET-positive states, but not those with entirely low AmFRET (**Figure 1B and S1E**). As predicted, the assemblies of DFDs that had transitioned discontinuously had fibrillar morphologies, whereas those that had transitioned continuously (low to high DAmFRET) instead mostly formed spherical or amorphous puncta (**Figure 1B, S1F-H**).

For discontinuous DFDs, the soluble protomers in the low FRET cells are hypothetically poised to assemble; they just lack a structural template to get them started. We tested this hypothesis by co-expressing genetically encoded "seeds" (**Figure 1D-E**),[12] and found that the seeds caused cells to switch to the high AmFRET population for most discontinuous DFDs but not continuous DFDs **(Figure 1F, S1I, Table S1)**. We further demonstrated that assembly is more consistent with native DFD subunit interfaces than amyloid-like misfolding (**Supplemental Information, Figure S2A-B**). This distinction is important because amyloid is the only other form of assembly that has been experimentally shown to be capable of forming a discontinuous DAmFRET profile.[16,26] Altogether, these data confirm that a subset of DFDs can supersaturate in a soluble form to power subsequent switch-like assembly.

The magnitude of supersaturation in vivo is determined by the ratio of a protein's total concentration to its C_{sat}, which reflects the strength of interactions between subunits in its assembled structure.[27] Total concentration and C_{sat} can evolve independently by gene regulation and DFD sequence, respectively. Consequently, if the function of discontinuous DFDs involves supersaturation, we would expect evolution to have lowered their C_{sat} while raising their expression relative to continuous DFDs. To test these predictions, we first analyzed the relationship of nucleation barriers to C_{sat}, as determined by each protein's transition concentration in the presence of seed. As expected, discontinuous DFDs exhibited lower C_{sat} values than continuous DFDs (**Figure 1G, Table S1**), and in the absence of seed achieved soluble concentrations that exceeded them by at least four-fold on average (**Figure 1H**).

Nucleation barriers are restricted to innate immune signalosome adaptors

We next evaluated the relationship of nucleation barriers to DFD concentrations in vivo. Using published proteomic datasets,[28–30] we found that proteins with discontinuous DFDs tend to be expressed more abundantly than those with continuous DFDs, both at the cell type and tissue levels (**Figure 2A, S3A-B and Table S1**). We then used a high-coverage transcriptomics dataset[31] to ask how C_{sat} values relate to DFD gene expression in primary immune cells. Remarkably, transcript abundances significantly anticorrelated with C_{sat} in 17 of the 18 canonical immune cell populations (**Figure 2B and S3C**). Such a relationship is highly unusual for soluble proteins, whose expression instead tends to strongly correlate with C_{sat}.[32] These analyses collectively indicate that discontinuous DFDs are likely to be functionally supersaturated in their endogenous physiological contexts.

Given that nucleation barriers are restricted to only a subset of DFDs, we asked if the DFDs with nucleation barriers tend to have different signaling roles than those without. From our prior demonstrations of prion-like activity by ASC, MAVS, and BCL10,[12,33] we suspected an enrichment among adaptors. However, DFD proteins have not been systematically evaluated with respect to adaptor function. We therefore focused on the defining property of "adaptors"

physically connecting other proteins by quantifying their centrality in the DFD protein-protein interaction network. Proteins with high "degree centrality" are hub-like, with many direct interactions. Proteins with high "betweenness centrality" lie on the shortest paths between other nodes and therefore act as bottlenecks in the network. Assessing both measures (see methods), we observed that discontinuous and/or seedable DFD proteins have significantly greater degree and betweenness centralities (**Figure 2C and S3D-E**). As a point of comparison, we performed the same analysis for the domain family most closely resembling DFDs -- Sterile Alpha Motif (SAM). SAM domains have similar size, structure, number (76 in humans), and function as DFDs, often serving as polymeric scaffolds of signaling complexes.[34–36] Unlike DFDs, however, SAM domains cannot supersaturate.[24] Consistent with that, we found that they also have much lower betweenness centrality in their physical interaction network as compared to discontinuous DFDs ($p = 0.0003$; **Figure S3F**).

For a DFD nucleation barrier to enable on-demand assembly, the DFD must remain supersaturated even as a full-length (FL) protein. This means that other parts of the protein must not trigger nucleation prematurely, as through homo-oligomerization. Nor should they disfavor the assembled state, which would raise C_{sat}. We therefore evaluated the phase behaviours of 21 diverse DFD-containing FL multidomain proteins. Most of the proteins behaved the same way as their respective DFDs (**Figure 2D, Figure S4A, and Table S2**). Six proteins suppressed the ability of their DFDs to supersaturate, resulting in continuous low or moderate DAmFRET, suggesting they form non-nucleated oligomers. To determine if the DFDs are in an active polymer configuration within these oligomers, we tested the ability of FL NLRP3 to nucleate its cognate adaptor, ASC. It failed to do so (**Figure S4B**), revealing that the oligomers are "autoinhibited" as has been previously demonstrated for multiple DFD-containing receptors and effectors.[9,37–43] This implies that the DFD within FL NLRP3 (and presumably other DFDs that lost supersaturability in their FL context) cannot *self*-assemble; instead, its joining the polymer structure is driven by the energy released by ligand (e.g. D/PAMP) binding. This stoichiometric requirement limits spurious activation that would otherwise kill or inflame cells unnecessarily.[9,37–42] In contrast to these autoinhibited proteins, five of the FL proteins instead retained or enhanced their DFDs' nucleation barriers: ASC, BCL10, FADD, MAVS, and TRADD (**Figure 2D, Figure S4A, and Table S2**). Testing a subset of FL proteins further, we found that only this latter group can be self-seeded (**Figure S5A**). These proteins collectively span all four DFD subfamilies, and all of them function as major adaptors in innate immune signalosomes (**Figure 2E)**. ASC, BCL10, MAVS, and TRADD drive inflammation and/or inflammatory cell death downstream of D/PAMP sensing.[44–50] FADD signals downstream of death ligands and certain D/PAMPs through various signalosomes that can be either anti- or pro-inflammatory.[51–56] In contrast, signalosomes with primarily non-immunity functions -- the apoptosome, the PIDDosome, and the ectodysplasin (EDA) receptor complex[57–59] -- lacked supersaturation (**Figure 2G**). Consistent with their functioning through supersaturation, only the innate immune set of adaptors are more abundantly expressed than their cognate receptors in the

human body (**Figure 2F**). These data collectively identify the adaptors, specifically, of inflammatory signalosomes as energy reservoirs for signal amplification.

Nucleation barriers may facilitate signal amplification in human cells

To explore the functionality of supersaturation, we focused on two modes of programmed cell death signaling that differed in this regard: intrinsic apoptosis and pyroptosis. The former occurs downstream of persistent intracellular stresses.[60–62] The latter is instead triggered by minute levels of D/PAMPs and therefore involves greater signal amplification. Our DAmFRET analyses revealed that CARDs of the apoptosome lack nucleation barriers whereas CARDs of the inflammasome, which drives pyroptosis, have nucleation barriers (**Figure S6A**).

To test if the absence of nucleation barriers limits the sensitivity of the apoptosome, we adapted an optogenetic approach[12,63–65] to precisely control the initiation of intrinsic apoptosis. HEK293T cells lack the inflammasome constituents NLRC4, ASC, and CASP1, allowing us to repurpose their DFDs in this cell line. Accordingly, we transduced the cells with mScarlet-I fusions of either the non-supersaturable WT apoptosome effector, CASP9, or a chimeric version that harbored the supersaturable DFD of CASP1 in place of its own ($CASP9^{CASP1CARD}$). We simultaneously transduced the cells with blue light-inducible seeds of the cognate upstream DFDs -- opto-APAF1 or opto-NLRC4, respectively (**Figure 3A**). We then assessed signal propagation through the reconstituted pathways by measuring activation of CASP9's downstream target, CASP3/7, after one minute of blue light stimulation. Both cell lines activated a fluorescent CASP3/7 reporter to the same extent (**Figure 3B**), confirming that the different modifications do not sterically interfere with the proteins' activities.

To now assess signal amplification, we evaluated both the persistence of DFD assemblies and their ability to commit cells to apoptosis following an otherwise sublethal stimulus. We anticipated that cells expressing non-supersaturable CASP9 will 1) form transient clusters and consequently 2) survive a short blue light stimulus. In contrast, cells expressing supersaturable CASP9 will 1) form perdurant clusters that signal indefinitely, and consequently 2) die even after a short blue light stimulus.

To test prediction 1, we stimulated the cells with blue light for one minute and monitored subsequent protein localization. We found that both pairs of proteins formed puncta in essentially all cells within one minute (**Figure 3C-D; Movie S1**). The puncta with non-supersaturable CASP9 then dissolved over the course of the next 10 minutes. In contrast, the puncta with supersaturable CASP9 instead continued to grow at a constant rate for at least the next 20 minutes (**Figure 3C-D; Movie S2**), confirming that the protein's drive to polymerize exists even without the stimulus.

To test prediction 2, we measured cell death two hours after the initiation of blue light stimulation for either one minute or the entire two hours. Neither pair of proteins induced cell

death in the absence of blue light (**Figure 3E**). Non-supersaturable CASP9 induced death in approximately 18% and 55% of cells following the short and long stimulation, respectively (**Figure 3E**), confirming the expected dose-dependence of signaling. In contrast, supersaturable CASP9 induced death in most cells even upon short stimulation, consistent with the expected amplification of signaling due to supersaturation-mediated DFD polymerization. We note that the increased stability of NLRC4^{CARD} and CASP1^{CARD} polymers relative to APAF1^{CARD} and CASP9^{CARD} oligomers could increase signal amplification irrespective of polymerization however, due to the slower dissolution of assemblies that formed even during stimulation, which would give CASP9^{CASP1CARD} more time to activate more molecules of CASP3/7. Consequently, further work will be required to distinguish the contributions of each mechanism to amplification.

Some innate immune adaptors are endogenously supersaturated

We next asked if pyroptosis and extrinsic apoptosis are indeed powered by adaptor supersaturation in vivo. We first induced pyroptosis in human THP-1 monocytes by treating them with poly(dA:dT), a ligand for the inflammasome receptor, AIM2. By 18 hours, approximately 70% of the cells were dead or dying. We then deleted *PYCARD* to determine if cell death depended on ASC, the adaptor for the inflammasome. Death was delayed, but not eliminated (**Figure 4A**). We then also deleted *FADD*, encoding an adaptor that has been shown to co-assemble with AIM2 in pathogen-triggered PANoptosis.[66] Death was reduced further still (**Figure 4A and S6B**), confirming that AIM2 activation can induce cell death through both ASC and FADD.

To eliminate the potentially confounding effects of orthogonal dsDNA sensors,[67] we next placed AIM2^{PYD} under blue light control and confirmed that the resulting fusion protein -- "opto-AIM2" -- grants direct control over seed formation (**Figure 4B and 4C, top**). Using this system, a transient blue light exposure induced AIM2 clustering within seconds and cell death within ten minutes (**Figure 4C-D and Movie S3-S4**). Next, we evaluated if cell death depended on ASC or FADD. We found that stimulating WT cells with a one-second blue laser pulse every 15 minutes killed essentially all of them within one hour (**Figure 4E**). In contrast, only half of cells lacking ASC (*PYCARD*-KO) died, and they did so with delayed kinetics consistent with FADD-driven signaling.[52,68,69]

Finally, we directly assessed inflammasome nucleation by AIM2^{PYD} seeds. To do so we reconstituted the *PYCARD*-KO with mScarlet-I-tagged ASC and titrated its expression to well below endogenous levels so as to circumvent any potential for the fusion tag to enhance the protein's oligomerization (although this would be unexpected;[70] **Figure S6C-E**). We then tracked AIM2^{PYD} and ASC localization following a 10-second laser pulse. Both proteins began to cluster almost immediately. AIM2^{PYD} cluster growth nearly stopped by three minutes, consistent with excited Cry2 relaxation on a similar time scale.[63,71] In contrast, ASC clusters

continued rapid growth for more than ten minutes (**Figure 4F**), demonstrating that their drive to do so is independent of the triggering stimulus. The plasma membrane concomitantly permeabilized as a result of gasdermin D (GSDMD) activation,[72] and to an extent that increased with the level of ASC expression (**Figure 4G**). These data collectively confirm that endogenous ASC is highly supersaturated prior to stimulation, and that the extent of supersaturation determines the extent of signal amplification.

Given that inflammatory signalosomes frequently initiate programmed cell death, and that a kinetic barrier governs their activity, the susceptibility of cells to aberrant cell death through spontaneous nucleating fluctuations is expected to increase with the level of adaptor supersaturation in vivo. This would constrain a cell's life expectancy if such nucleation occurs with appreciable frequency. To explore this possibility, we asked how adaptor supersaturation (as approximated by the ratio of mRNA levels to C_{sat} values) relates to the turnover rates of each cell type in the human body.[73] We found that short-lived cells such as monocytes indeed have greater DFD supersaturation than long-lived cells such as neurons (**Figure 4H**). Among individual DFD proteins, cell turnover correlated especially strongly with the expression level of ASC (**Figure S6F-G**), suggesting that life expectancy may be limited by the thermodynamic drive for inflammatory signal amplification.

The nucleating interactome is highly specific

DFDs share the same fold and are co-expressed in many of the same cells. While spontaneous nucleation of supersaturable DFDs poses an inherent risk of inadvertently activating end fate cell signalling, this possibility is multiplied by the risk of cross-activation between DFDs in different pathways. To what extent do they nucleate each other? To determine specificity and systematically map the nucleating interactome of DFDs, we mated our library of seed-expressing yeast strains with a library of strains expressing each mEos3-fused DFD (**Figure S7A**) to create over 10,000 arrayed diploid yeast strains that we then screened by DAmFRET (**Figure S7B and C**).

In total, we identified 171 nucleating interactions, representing just ~1.6% of the total library (**Figure S7D-F and Table S4**). The interactions were largely constrained not just to members of the same subfamily, but to members of the same signaling subnetwork even within subfamilies (**Figure 5A-B**). For example, CARDs of the CBM signalosome nucleated each other but not CARDs of the inflammasome, and vice versa. As an exception, PYDs of the inflammasome and DEDs of the Death-Inducing Signaling Complex (DISC) nucleated each other (**Figure 5C**). These interactions are consistent with the residual cell death we observed in the *PYCARD FADD* double knockout, as well as previously observed crosstalk between these pathways and the close phylogenetic relationship between PYDs and DEDs.[69,74–76]

On the whole, the observed network of nucleating interactions reveal that DFDs from different pathways generally function independently of each other, allowing adaptors to serve as orthogonal energy reservoirs for their respective signalosomes (as schematized in **Figure 2E**).

DFD nucleation barriers are deeply conserved

Animals acquired DFDs horizontally from bacteria,[5,77,78] giving rise to an ancestral DISC (conserved across metazoa) and later inflammasome (conserved across vertebrates; **Figure 6A**).[79,80] To investigate conservation of nucleation barriers, we characterized by DAmFRET the phase behaviours of DFD-containing constituents of a basal inflammasome -- NLRP3, ASC, and CASP1 from zebrafish (*Danio rerio*); and a basal DISC -- A0A1X7U321, FADD, and CASP8 from the model sponge, *Amphimedon queenslandica*. As for their human counterparts, the fish and sponge adaptors -- but not the receptors and effectors -- were supersaturable (**Figure 6B and S8A-B**). These results suggest that the function of DFDs as energy reservoirs preceded the radiation of animals.

Discussion

Our systematic investigation revealed that metastable supersaturation of a select subset of adaptor proteins provides an energetic basis for DFD-mediated signal amplification.

Seminal studies on the structures of DFDs have led to the common view that DFDs generally function as homotypic interaction modules.[9,81] We were therefore surprised to find that approximately half (51) of human DFDs failed to detectably self-assemble even when expressed well-beyond physiological concentrations. This suggests that a large fraction of DFDs function through hetero- rather than homo-oligomerization. From known examples we postulate these will involve 1) receptors templating adaptor nucleation, 2) effectors binding to adaptor polymers, and 3) regulators repressing signaling by competing with 1 and 2.[82–85] Importantly, and despite a general appreciation that DFD polymerization functions to amplify signaling, most of the DFDs that self-assembled (36 of 57) lacked sufficient nucleation barriers to supersaturate at the cellular level. This precludes them from amplifying signals without additional energy expenditure by the cell. The only DFDs to supersaturate in full-length protein contexts were adaptors of inflammatory signalosomes. The sparsity of this property belied its functional importance, however, as indicated by higher centrality measures. Generally, the more central proteins of networks tend to be essential,[86] more abundant,[87] slower evolving,[88] and more frequently targeted by pathogens than noncentral proteins.[87,89] Examining the topology of DFD networks revealed a core set of signal amplifying adaptors each interacting with a sequence-specified set of receptors, effectors, and regulators that categorically lack nucleation barriers. Because nucleation involves only a tiny fraction of the supersaturated adaptors, they are poised to amplify minute signals from their cognate receptors and transduce them to their cognate effectors, precisely as required for innate immunity. Furthermore, because this attribute is conserved across

homologous animal adaptors, energy storage for on-demand signaling may be an ancestral function of DFDs.

If supersaturation is indeed important for innate immune signaling, why are so few DFDs supersaturable? The answer may lie in the fact that each supersaturated node in a death-inducing pathway imposes a risk of unintentional death. We speculate that evolution therefore minimizes the number of supersaturated DFDs by restricting them to only the central nodes of the network. In this way, a restricted number of supersaturable DFDs can be continuously "repurposed" with receptor and effector proteins specific to each D/PAMP and mode of cell death.

Two prominent inflammatory signaling adaptors -- MyD88 and RIPK1 -- defied the broader trend in their inability to supersaturate. Intriguingly however, each functions in series with other adaptors that *do* supersaturate. MyD88 typically functions downstream of TIRAP,[90] whose TIR domain drives nucleation-limited polymerization in vitro and in cells.[91] Similarly, RIPK1 acts in conjunction with TRADD leading to either NF-κB activation, apoptosis (via FADD), or necroptosis (via RIPK3). TRADD and FADD were shown here to supersaturate, while RIPK3 contains an amyloid-forming motif (RHIM) whose self-assembly is required for necroptosis.[92] Hence, all of the partner adaptors of MyD88 and RIPK1 are either demonstrably or plausibly supersaturable, thereby obviating such functionality in MyD88 and RIPK1. Consequently, these exceptions in fact support the generalization that each inflammatory pathway has approximately one supersaturable node. Alternatively, MyD88 may be a false negative in our experiments, perhaps due to an absence of a required factor in yeast cells or the presence of a nucleating factor that does not exist in human cells. Unlike other adaptors which are effectively monomeric prior to activation, MyD88 forms discrete oligomers that activate by clustering into larger assemblies.[93–95] DAmFRET may be unable to resolve the transition between these multimeric forms. MyD88 was previously found to exhibit a nucleation barrier in vitro,[96] and to form switch-like and persistent assemblies at the subcellular level in vivo.[95,97]

We liken supersaturated DFD adaptors to 'phase change materials' in industrial thermal batteries, accumulating potential energy for subsequent deployment upon nucleation.[98,99] This differs fundamentally from signaling cascades that rely on chemical fuels like ATP. While ATP is a common good shared across cellular processes, DFD batteries are autonomous power sources, exclusive to each signaling pathway and therefore insulated from other cellular processes. This could allow for signal transduction independently of variable or compromised cell metabolism. Just as a battery cannot recharge itself, the DFD assemblies are effectively irreversible, committing the cell to terminal responses like death. This battery function rationalizes DFD prevalence over more common assembly modes like liquid-liquid phase separation (LLPS; **Figure 6C**). While LLPS offers sensitivity that can enhance D/PAMP detection,[100,101] the sharp drop in its nucleation barrier with increasing supersaturation[102–104] makes it unsuitable for long-term, high-energy storage needed for explosive signal amplification through rapid assembly.

Signalosome effectors activate through simple induced-proximity mechanisms that lack specific structural requirements of the DFDs themselves,[12,64,105,106] which suggests that the structures of DFD polymers are determined by a function of the solution phase *prior to activation*. Our finding that the function is energy storage rationalizes the strikingly regular structure of DFD polymers. The evolution of this function would have been driven by selection *against* premature assembly, favoring paracrystalline ordering whose infrequent nucleation allows for energy storage over a cell's lifetime. This differs from selection *for* a specific functional polymer structure, as seen for example in microtubules. This principle may also explain the functional substitution of DFDs with alternative paracrystalline modules like TIR domains and amyloids in some innate immune signaling pathways,[8] as well as the dearth of non-nucleated polymers, such as those of SAM domains, in innate immune signaling despite their prevalence in other signaling pathways.[34]

Despite functional nucleation barriers potentially driving the evolution of DFD polymerization, we emphasize that nucleation barriers are directly determined by the soluble ensembles that precede polymers. Our finding that only a subset of polymerizing DFDs exhibit nucleation barriers underscores this fact. These non-nucleation-limited polymers presumably have larger energetic differences between their orthogonal interfaces than those of nucleation-limited polymers, which would be expected to reduce the cooperativity of nascent polymer formation.[107] Fully elucidating the DFD structure-function relationship will require future exploration of the conformational preferences of monomers and early stage oligomers.

The ability of a protein fold to crystallize has few structural constraints, allowing relatively small changes in sequence to produce orthogonal signaling modules. The resulting evolvability may be essential in the never-ending arms race against pathogens. High specificity also insulates pathways from each other and from cellular processes and metabolic fluctuations that could aberrantly activate them to lethal consequence.[108–110] The precise determinants of specificity will differ for each interaction, but prior work has uncovered principles that will likely prove general, such as the shape and electrostatic complementarity of interfaces and cross-compatibility of the polymers' helical architectures.[23,83,111–113]

Our findings imply that cells perpetually await death. The theoretical cumulative certainty of stochastic nucleation over time appears to be reflected in the observed relationship of DFD supersaturation to mortality rates across human cell types. We speculate that this underpins a fundamental tradeoff between innate immunity and life expectancy, potentially contributing to age-related inflammation and stem cell exhaustion[114].

Limitations of the study

Multiple DFDs were found to populate stable ordered polymers in all cells. Although we did not observe a nucleation barrier for these, it is possible that they are supersaturable in vivo at much lower than the micromolar concentrations surveyed by DAmFRET. Similarly, a small number of

DFDs that populated only a low AmFRET state did not express to high concentrations in yeast, and it is possible that they can self-assemble under cellular contexts that allow them to reach higher concentrations.

Our study necessarily simplifies and abstracts human innate immune signaling. We considered the cytoplasm of living yeast cells to be a suitable proxy for the physiological context of DFDs *as a whole*, while acknowledging that the endogenous contexts of DFDs differ from that in our experiments. For example, several of the DFDs normally localize to membranes or the nucleus in human cells, and this could impact their phase behavior. Nevertheless, we find no evidence that such localizations would reduce supersaturation, as none of the DFDs from nuclear proteins exhibited nucleation barriers in our experiments. Likewise, in the case of MAVS, which normally localizes to the mitochondrial membrane, we found that the FL protein (containing its mitochondrial localization signal) was more supersaturable than its DFD alone, suggesting that localizing the protein to the mitochondrial surface increases the nucleation barrier despite restricting its diffusional entropy and increasing its local concentration. Our work also does not explore the many ways that DFD assembly can be regulated transcriptionally and post-translationally. For example, NLRP3 is upregulated and becomes phosphorylated in response to LPS "priming" of the inflammasome,[115] and polyubiquitination of RIG-I promotes its activation of MAVS.[116] Such modifications imply that some signal amplification can occur upstream of supersaturated adaptors. The level of adaptor supersaturation differs between cell types (as we have shown) and is also likely to be dynamically regulated.

Figure legends

Figure 1. **A select subset of DFDs have intrinsic nucleation barriers enabling persistent supersaturation**

A. Schematic diagram illustrating two models for signal amplification through protein self-assembly. **Top left:** Extrinsic model, where D/PAMP-binding coupled with nucleotide hydrolysis stabilizes active assemblies (red glow) relative to solute precursors (blue glow). This model is exemplified by localized actin polymerization downstream of many cell surface receptors,[117] but could also occur indirectly by, for example, phosphorylation-mediated release of solubilizing factors. **Bottom left:** DFDs that function in this way will assemble promptly and monotonously above their saturation concentration (C_{sat}). **Top right:** Intrinsic model, where the protein is supersaturated at rest but prevented from assembling by a sequence-encoded nucleation barrier. D/PAMP-binding eliminates the barrier, releasing the energy of supersaturation to drive assembly. The models are not mutually exclusive. **Bottom right:** DFDs that function in this way will remain soluble above C_{sat} until stochastic nucleation, creating a discontinuous relationship of assembly to concentration across a population of cells.

B. Illustration showing how the concentration-dependence of self-assembly as classified by DAmFRET relates to the subcellular morphology of self-assemblies classified by high-throughput confocal microscopy. “Continuous” and “discontinuous” classifications describe the relationship of self-assembly (AmFRET, y-axis) to expression level (x-axis) for each DFD. Discontinuous DFDs exhibit a range of concentrations where self-assembly occurs stochastically, indicating an intrinsic nucleation barrier. The four instances of visible assemblies despite no AmFRET-positive cells are presumed to result from those DFDs partitioning with other cellular components or endogenous condensates wherein they remain too dilute to FRET. Cells in the matrix are colored according to the log2 ratio of observed to expected frequencies. The indicated p-values (adjusted for multiple hypotheses) were obtained with an exact multinomial test using the total frequencies of each morphology.

C. Distribution of DAmFRET classifications across the four subfamilies of DFDs.

D. Schematic diagram of our experimental design to assess the ability of each DFD to seed itself. Top: Biological activation of an exemplary signalosome -- the AIM2 inflammasome -- occurs when the receptor AIM2 oligomerizes on the multivalent PAMP, dsDNA, and then templates the assembly of the adaptor protein, ASC. Bottom: Experimental paradigm to test for supersaturation mimics biological activation, by expressing each DFD in trans with the same DFD expressed as a fusion to μNS, a modular self-condensing protein. AmFRET-positivity will only occur if the μNS fusion templates subsequent self-assembly by the non μNS-fused DFD.

E. Representative DAmFRET data contrasting two self-assembling DFDs -- one that is supersaturable (left) and the other that is not (right). The plot for the supersaturated protein exhibits a discontinuous distribution of AmFRET across the expression range (top

and bottom). The discontinuity is eliminated, with all cells moving to the AmFRET-positive population, by expressing the protein in the presence of genetically encoded seeds (middle). The dashed horizontal lines approximate the mean AmFRET value for monomeric mEos3. Procedure defined units (p.d.u.).

F. Contingency table showing that discontinuous DFDs tend to be self-seedable. Each DFD was co-expressed with an orthogonally fluorescent μNS-fused version of the same DFD. Fisher's exact test revealed an association between continuity and self-seedability ($p < 0.001$).

G. Boxplot comparing the C_{sat} values (as approximated by $C50_{seeded}$) of continuous and discontinuous DFDs. Discontinuous DFDs have significantly lower C_{sat}, indicating greater stability of the assemblies. Mann-Whitney U = 457, $n_{continuous} = 26$, $n_{discontinuous} = 20$ ($p < 0.001$).

H. Boxplot comparing supersaturability, represented as the fold change reduction in C50 by seeding ($C50_{stochastic}$ - $C50_{seeded}$), of continuous and discontinuous DFDs. The C50 values were more strongly reduced by seeding for discontinuous DFDs than for continuous DFDs. Mann-Whitney U = 164, $n_{continuous} = 58$, $n_{discontinuous} = 21$ ($p < 0.001$).

See also Figures S1, S2, S5 and Table S1.

Figure 2. **Nucleation barriers are a characteristic feature of inflammatory signalosome adaptors**

A. Boxplot of DFD-containing protein abundances in monocytes, showing that discontinuous DFDs have higher endogenous expression levels. Mann-Whitney U = 53, $n_{continuous} = 26$, $n_{discontinuous} = 8$ ($p = 0.039$). Protein abundance values are from PAXdb.[28]

B. Scatter plot of DFD gene expression in monocytes (normalized transcripts per million) and C_{sat} values. Spearman R = -0.285 ($p = 0.03$). Adaptor DFDs are labeled. Dataset obtained from the Human Protein Atlas.

C. Top: box plots of degree centrality (left) and betweenness centrality (right) of continuous and discontinuous DFDs in the endogenous network of physically interacting DFD proteins, showing that the latter are more centrally positioned. Degree centrality Mann-Whitney U = 242.0 ($p = 0.010$); betweenness centrality Mann-Whitney U = 274.0 ($p = 0.030$); $n_{continuous} = 46$, $n_{discontinuous} = 18$. Bottom: box plots of centrality measures of non-seedable and seedable DFDs, showing that the latter are more centrally positioned. Degree centrality Mann-Whitney U = 167.5 ($p = 0.022$); betweenness centrality Mann-Whitney U = 172.5 ($p = 0.023$); $n_{non\text{-}seedable} = 35$, $n_{seedable} = 16$.

D. Visualization of how the DAmFRET profiles of isolated DFD domains (left) change in their full-length contexts (right), showing that only adaptor proteins (green connections) tend to retain discontinuous transitions in their full-length context.

E. Subnetworks of prominent signalosome adaptor proteins that were found to be supersaturable. Edges connect nodes with experimentally determined physical

interactions with confidence > 0.9 in STRING. All proteins shown have DFDs except TRAFs. Each adaptor's node size is proportional to its supersaturability score.

F. Comparison of protein abundances at the whole body level for the signalosome components in Figure 2E (left) and Figure 2G (right), showing that adaptors are more highly expressed for the former. Protein abundance values are from PAXdb.[28] P-values are from Mann-Whitney test. For supersaturable signalosomes: $n_{sensor} = 13$, $n_{adaptor} = 6$, $n_{effector} = 4$; sensors and adaptors, $U = 4.0$ ($p < 0.001$); sensors and effectors, $U = 6.0$ ($p = 0.023$); adaptors and effectors, $U = 18.0$ ($p = 0.257$). For non-supersaturable signalosomes: $n_{sensor} = 3$, $n_{adaptor} = 2$, $n_{effector} = 2$; sensors and adaptors, $U = 1.0$ ($p = 0.400$); sensors and effectors, $U = 0.0$ ($p = 0.200$); adaptors and effectors, $U = 0.0$ ($p = 0.333$).

G. Subnetworks of signalosomes lacking supersaturable DFDs. Edges connect nodes with experimentally determined physical interactions with confidence > 0.9 in STRING. All proteins shown have DFDs except TRAF6.

See also Figures S3, S4 and S5, and Tables S1 and S2.

Figure 3. **Nucleation barriers may facilitate signal amplification in human cells**

A. Schematic diagram of experiment in HEK293T cells to reconstitute the apoptosome with optogenetic control, in either a non-supersaturable or supersaturable format. The non-supersaturable format comprises CASP9 activated by $APAF1^{CARD}$ (as in the native apoptosome); the supersaturable format comprises chimeric CASP9 with $CASP1^{CARD}$ replacing $CASP9^{CARD}$ ($CASP9^{CASP1CARD}$), activated by chimeric APAF1 with $NLRC4^{CARD}$ in place of $APAF1^{CARD}$. Blue light triggered assembly in both cases, but subsequent continued assembly in the dark only occurred for the supersaturated format.

B. Caspase 3/7 activity reporter fluorescence intensities in the absence of stimulation or after one minute of 488 nm stimulation for cell lines expressing the non-supersaturable or supersaturable pairs, showing that both pairs comparably activate caspase 3/7 while oligomerized. $APAF1^{CARD}$-Cry2 + CASP9-mScarlet-I, dark n = 163, pulse n = 375, Mann-Whitney $U = 11362$ ($p < 0.0001$). $NLRC4^{CARD}$-Cry2 + $CASP9^{CASP1CARD}$, dark n = 46, pulse n = 305, Mann-Whitney $U = 4253$ ($p < 0.0001$).

C. Coefficient of variation (CV) of fluorescence distribution in HEK293T cells expressing the indicated protein pairs after a single one minute 488 nm laser activation. Top, $APAF1^{CARD}$-Cry2 and CASP9-mScarlet-I display rapid cluster formation that dissociates by 20 min. Bottom, $NLRC4^{CARD}$-Cry2 and chimeric $CASP9^{CASP1CARD}$ cluster less rapidly but the clusters continue to grow indefinitely.

D. Representative images from experiment in C. Clusters of $APAF1^{CARD}$-Cry2 and CASP9-mScarlet-I form then dissociate while $NLRC4^{CARD}$-Cry2 and $CASP9^{CASP1CARD}$ crusters only get larger.

E. Quantification of cell death of the HEK293T chimeric cells (as in A) using Annexin V-Alexa 488 staining, either two hours after a single one minute pulse of 488 nm laser, or

after two hours of "constant" stimulation whereby cells were subjected to a one second pulse every one minute. P-values derived from t-test.

See also Figure S6, Table S3 and Movie S1, S2.

Figure 4. **Innate immune adaptors are endogenously supersaturated**

A. Time course of apoptotic cell death of THP-1 cells following exposure to AIM2 ligand, poly(dA:dT). P-value obtained from ANOVA followed by pair comparison.
B. Schematic diagram of the experiment to transiently optogenetically stimulate $AIM2^{PYD}$ to monitor ASC^{PYD} assembly. This experiment was conducted in HEK293T cells because they do not undergo pyroptosis.
C. Top, Time course of fluorescence intensity distribution in THP-1 cells following 10 seconds of optogenetic activation, showing that WT $AIM2^{PYD}$ forms clusters (high CV) that persist and induces cell death, while the F27G solubilizing mutant[23] forms clusters that subsequently disperse. Bottom, normalized Sytox Orange fluorescence intensity for the experiment in the top panel.
D. Representative confocal microscopy images from a timelapse of THP-1 monocytes showing that transient optogenetic stimulation of WT but not F27G mutant of $AIM2^{PYD}$ causes it to form puncta that coincide with cell death. Sytox Orange was used for this experiment because it can be excited without activating Cry2.
E. Time course of cell death of THP-1 cells when subjected to a blue light pulse every 5 minutes ("repeated"), showing rapid cell death (violet trace) only when $AIM2^{PYD}$ is WT and when ASC is present. The absence of ASC results in slower death (green trace), consistent with apoptosis. The F27G mutation of $AIM2^{PYD}$ blocks cell death irrespective of ASC (black and golden traces).
F. Coefficient of variation (CV) of fluorescence distribution of $AIM2^{PYD}$-Cry2 and ASC-mScarlet-I in THP-1 *PYCARD-KO* cells following a 10 s blue light pulse. This shows that $AIM2^{PYD}$ and ASC-mScarlet-I (with slightly delayed kinetics) rapidly form clusters that persist well after stimulus removal. ASC-mScarlet-I was induced to only ~20% of the ASC expression in WT cells using 1.0 µg/mL doxycycline (dox).
G. Quantification of CellTox staining in individual ASC-mScarlet-I THP-1 *PYCARD-KO* cells 30 minutes after a 10 second blue laser pulse, at different levels of dox-induced ASC-mScarlet-I expression. Green dotted line indicates 95% confidence interval (CI) for background fluorescence intensity, above which cells were considered CellTox-positive. Error bars denote standard deviation. Control, n = 37. 0.25 µg/mL dox, n = 36. 0.5 µg/mL dox, n = 47. 0.75 µg/mL dox, n = 113. 1 µg/mL dox, n = 180.
H. Top: The metastability of supersaturation implies that cells will occasionally inflame and/or die from stochastic (without D/PAMPs) DFD nucleation, which creates a tradeoff between innate immunity and life expectancy. Bottom: Scatter plot showing the relationship between geometric mean of adaptor supersaturation including ASC, FADD, BCL10, TRADD, MAVS (as approximated by the ratio of transcription levels and C_{sat}

values) and mean lifespan for each cell type in the human body for which data is available.[73] Cell types with greater DFD supersaturation have shorter mean lifespans. The red line represents the best-fit power-law regression, obtained by performing linear regression in log-log space. The shaded region represents the 95% confidence interval for the trend line. Spearman R = -0.8375 (two-tailed p = 0.000027).

See also Figure S6 and Table S3.

Figure 5. **The nucleating interactome is highly specific**

A. Matrix of all nucleating interactions (gray-shaded circles) detected in a comprehensive DAmFRET screen of > 10,000 DFD pairs. Each DFD-mEos3 (columns) was separately expressed with each DFD-μNS seed (rows). Darker shading of the circle denotes increased seedability. Interactions among members of the same signaling pathway (in legend) appear in color shaded squares. Asterisk denotes seeds that were screened in a separate experiment from the rest. The matrix was clustered on seedability values, on a log scale, using the SciPy.cluster.hierarchy v1.11.1 linkage and dendrogram Python packages, using the Ward variance minimization algorithm to calculate distances. Procedure defined units (p.d.u.).
B. Circos plot of the nucleating interactions summarized by DFD subfamily. Each subfamily is represented with a segment proportional to the number of DFDs with a nucleating interaction, as indicated by ribbons within and between segments. Inner stacked bars around the perimeter show the numbers of DFDs in each subfamily seeded by the subfamily in that segment. Middle stacked bars around the perimeter show the numbers of DFDs in each subfamily that seed the subfamily in that segment. Outer stacked bars around the perimeter show total nucleating interactions involving the subfamily in that segment.
C. Nucleating interactions involving DFDs in extrinsic apoptosis and pyroptosis, with blue edges highlighting the direct nucleating effect of AIM2 on FADD and ASC that is explored in Figure 4. The network was created in Cytoscape with node size corresponding to betweenness centrality and grouped by reported function. Interactions between FL proteins (Table S2) were included. Edge darkness indicates the seedability score of the corresponding interaction.

See also Figure S7 and Table S4.

Figure 6. **DFD nucleation barriers are deeply conserved**

A. Phylogenetic tree illustrating evolutionary relationships between DFD signaling pathways from bacteria to humans.
B. DAmFRET classifications for DFD-only and FL components of the DISC from the model sponge, *Amphimedon queenslandica*, and of the inflammasome from the model fish *Danio rerio*, showing that adaptors are specifically supersaturable. **D. rerio* CASP1^{FL} exhibits a high C_{sat} in the mid-micromolar range, **D. rerio* CASP1^{FL} exhibits a

high C_{sat} in the mid-micromolar range based on prior calibrations of DAmFRET plots,[16] which greatly exceeds the nanomolar concentration expected for endogenous procaspase-1,[118] making it unlikely to supersaturate at endogenous concentrations.

C. Physical logic of DFD function. **Left:** Cells experience thermodynamic perturbations either from stochastic fluctuations (noise) or D/PAMP binding to innate immune receptors. These perturbations can nucleate supersaturated signaling proteins (dashed horizontal lines) with a probability that depends on the type of phase transition and specifically, whether it is accompanied by structural ordering. **Middle:** For phase separation in the absence of structural ordering (LLPS), the nucleation barrier ($\Delta\Delta G_{(nucleus - solute)}$) declines sharply with concentration beyond C_{sat},[103,119] which increases its susceptibility to noise. This limits the level of supersaturation that can be maintained by a cell (vertical dashed line), and therefore, the extent to which assembly ($\Delta\Delta G_{(solute -- assembly)}$) can power signal amplification (tiny battery schematic). **Right:** For phase separation with structural ordering (paracrystallization as in adaptor DFD assemblies), the dependence of nucleation on concomitant intramolecular fluctuations buffers the barrier against concentration (as indicated by a shallower curve relative to LLPS), which allows cells to maintain much higher levels of supersaturation.[16,21] Following nucleation, the assemblies grow and deplete soluble protein until it is no longer supersaturated, driving amplification (diagonal orange arrow) through proximity-dependent effector activation. The intrinsic nucleation barriers encoded by solution phase DFD ensembles therefore allow them to function as phase change batteries (giant battery schematic) to power innate immune signal amplification.

See also Figure S8 and Table S2.

Methods

Reagents and antibodies

Hygromycin B (Invivogen, ant-hg-1), Penicillin-Streptomycin (ThermoFisher, 1514014gp), PMA (BioVision, 1544-5), Puromycin (Invivogen, ant-pr-1), Sytox Orange (ThermoFisher, S11368), CellTox (Promega, G8741), Annexin V Alexa568 (1:200, ThermoFisher, A13202), Annexin V Alexa488 (1:200, ThermoFisher, A13201), Incucyte® Caspase-3/7 Dye (Sartorius, 4440). Antibodies, anti-ASC (Santa Cruz Biotechnology, sc-514414), anti-FADD (Sigma, 05-486), anti-Actin (Santa Cruz Biotechnology, sc-8432) were obtained from the indicated vendors.

Structural analyses

Twelve human proteins contain two DFDs, typically one closely following the other. To determine if the DFDs in such pairs should be evaluated independently or together, we used the predicted aligned error (PAE) matrix generated by AlphaFold3.[120] PAE is the expected positional error at residue x if the predicted and actual structures are aligned on residue y. Seven of the DFD pairs exhibited very low interdomain PAE scores comparable to those of the component DFDs (**Figure S1B,** bottom), suggesting a conserved fixed geometric relationship between the domains. We therefore considered these tandem DFDs as single members of their respective subfamilies. Similarly, we excluded the annotated[6] PYD-like domain of CENP-N because the PAE matrix and experimental structures show that it is in fact part of a larger non-DFD.

Plasmid construction

Yeast expression plasmids were made as previously described.[16] Briefly, we used a high copy episomal vector, V08, which contains inverted BsaI sites to support Golden Gate cloning, followed by a rigid helical linker 4x(EAAAR) and mEos3.1. This vector drives the expression of proteins from a *GAL1* promoter and contains the auxotrophic marker *URA3*. The vector V12 is identical to V08 except that mEos3.1 and linker precedes rather than follows the BsaI sites, for expressing proteins with an N-terminal fusion. Inserts were ordered as yeast codon-optimized GeneArt Strings (Thermo Fisher) flanked by Type IIs restriction sites for ligation between BsaI sites in V08 and V12. Fusions were made opposite the native N- or C-terminus of each DFD to minimize non-native steric effects. All other inserts were cloned into respective vectors via Gibson assembly between the promoter and respective tag. All plasmids were verified by Sanger sequencing. All expression plasmids are listed in **Table S1**.

Lentivirus vectors were as previously described.[12] Briefly, optogenetic constructs were cloned into pLV-EF1a-IRES-Hygro (Addgene #85134) which encodes a hygromycin B resistance cassette. To create lentiviral vectors expressing the the optogenetic constructs fused with miRFP670nano[121] and Cry2, the corresponding sequences of AIM2^{PYD}, APAF1^{CARD}, NLRC4^{CARD} were inserted via Gibson assembly into pLV-EF1a-IRES-Hygro. Finally, The doxycycline-controlled lentiviral vectors were cloned via Gibson assembly with the respective

coding sequences from PYCARD, CASP9, CASP1, and mScarlet-I into pCW57.1 (Addgene #41393). All lentivirus vectors are listed in **Table S3**.

Yeast strain construction

Unseeded DAmFRET experiments were conducted using strain rhy1713.[16] To create strains expressing DFD seeds, we first transformed AseI digests of each DFD plasmid along with a plasmid expressing Cas9 and a guideRNA targeting the *URA3* markers into rhy2153. This strain contains a genomic landing pad consisting of natMX followed by the *tetO7* promoter and counterselectable *URA3* ORFs derived from *C. albicans* and *K. lactis*, and stop-μNS-mCardinal as described.[12] Successful integration of the insert replaces the *URA3* marker with the gene of interest and fuses to the protein's C-terminus μNS-mCardinal, under the control of a doxycycline-repressible promoter. Transformants were selected for resistance to 5-FOA and validated for successful seed integration by detection of mCardinal expression using flow cytometry. The arrayed library of resulting strains was then mated to each of the rhy1713 strains expressing separate DFD-mEos3.1 fusions, by pinning each pair of strains together onto agar omnitrays containing SD-URA+NAT+dox media. The resulting colonies were then pinned into liquid SD-URA+NAT+dox for continued diploid selection and creation of glycerol stocks. The entire nucleating interaction screening consisted of 384 96-well plates.

DAmFRET assay preparation and data collection

We performed DAmFRET as previously described.[16] Briefly, single transformant yeast colonies were inoculated in 200 μL of SD-URA in a 96-well microplate well and incubated in a Heidolph Titramax platform shaker at 30°C, 1350 RPM overnight. Cells were washed with sterile water, resuspended in galactose-containing media, and allowed to continue incubating for approximately 20 h. Microplates were then illuminated for 25 min with 320–500 nm violet light to photoconvert a fraction of mEos3 molecules from a green (516 nm) form to a red form (581 nm). At this point, cells were either used to collect microscopy data or continue the DAmFRET protocol.

For the nucleating interaction screen, glycerol stock plates were pinned into liquid SD-URA without dox and incubated for 16 h at 30°C with 1350 RPM shaking overnight. We then resuspended cells in fresh SD-URA media and continued incubation for an additional 20 h. After this, we resuspended cells in SGal-URA and continued incubation for 20 h to induce protein expression. Finally, we resuspended cells in fresh SGal-URA for 4 h prior to DAmFRET data collection. The library was then consolidated into 96 384-well plates.

DAmFRET data were collected on a ZE5 cell analyzer cytometer. Autofluorescence was detected with 405 nm excitation and 460/22 nm emission; side scatter (SSC) and forward scatter (FSC) were detected with 488 nm excitation and 488/10 nm emission. Donor and FRET fluorescence were detected with 488 nm excitation and 425/35 nm or 593/52 nm emission, respectively. Acceptor fluorescence was detected with 561 nm excitation and

589/15 nm emission. For each well, we collected a volume of 13 μL, resulting in approximately 500,000 events per sample. Data compensation was done in the built-in tool for compensation (Everest software V1.1) on single-color controls: non-photoconverted mEos3.1 and dsRed2 (as a proxy for the red form of mEos3). For nucleating interactions, we included an additional channel for mCardinal intensity with 561 nm excitation and 670/30 nm emission.

DAmFRET data analysis

Data were processed on FCS Express Plus 6.04.0015 software (De Novo). Events were gated for single unbudded cells by FSC vs. SSC, followed by gating of live cells with low autofluorescence and positive donor and acceptor fluorescence. With the exception of $TNFRSF10A^{DD}$ (TRAIL-R1) (rhx2933) which failed to express with either its C- or N-terminus tagged, all expression plasmids were processed. Plots represent the distribution of AmFRET (FRET intensity/acceptor intensity) vs. acceptor intensity (protein expression).

We then analysed the data as previously described.[20] Briefly, FCS files were gated using an automated R-script running in flowCore. Before gating, the forward scatter (FS00.A, FS00.W, FS00.H), side scatter (SS02.A), donor fluorescence (FL03.A), and autofluorescence (FL17.A) channels were transformed using a logicle transform in R. Single cells were gated using FS00.A vs SS02.A and FS00.H vs FS00.W. These were gated for expressing cells using FL03.A vs FL17.A. Cells falling within these gates were then exported as FCS3.0 files for further analysis.

DAmFRET histograms were divided into 64 logarithmically spaced bins across a predetermined range large enough to accommodate all data sets. The upper gate values were determined for each bin as the 99th percentile of the DAmFRET distribution in that bin. We used the expression of mEos3.1 alone to delineate the region of a DAmFRET plot that corresponds to no assembly. For all samples, cells falling above this region are considered to contain protein assemblies (FRET-positive). The fraction of cells in the assembled population was plotted as a ratio to the total cells in the bin for all 64 bins. The gross fraction of such cells expressing a given protein is reported as fgate.

Determination of continuity

We initially attempted to classify each DAmFRET dataset as one-state or two-state, and discontinuous or continuous for the latter, using an algorithm previously developed for this purpose.[26] However, the algorithm invariably misclassified discontinuous datasets as "continuous" when the AmFRET level of the high FRET state changed with concentration, i.e. exhibited positive or negative slope as for FAS^{DD} and $CASP2^{CARD}$, respectively. Due to this limitation, we adopted a different method.

To determine the continuity of an adequately expressed plasmid, we analysed the distribution of AmFRET values about the transition region. To do so, we fit a spline to the median AmFRET values across binned concentrations that met a density cutoff defined by a minimum of 20 cells,

a minimum cell density of 500, and no more than 25% of cells being defined as an outlier. The bin density is measured by the number of cells divided by the interquartile range (IQR) of AmFRET values within that bin. The number of bins was determined using Scott's rule for number of bins in a histogram. The median AmFRET values were calculated for each bin, and then denoised using the Python SciPy.signal.sosfiltfilt, resulting in the spline fit. This was bootstrapped 100 times with the average of all bootstraps reported as the final spline fit. The resulting spline was used to determine the transition region. The transition point is defined as the concentration with the greatest change in AmFRET. Therefore, this value was calculated as the maximum of the first derivative of the fitted spline, using the numpy.diff package. The transition range is defined as the region between the maximum positive and negative rate of change, indicating where the transition between FRET states is starting and ending, respectively. The transition starting point is calculated as the maximum of the second derivative that lies before the transition point, and the transition endpoint is calculated as the minimum of the second derivative that lies after the transition point. This is done on all 100 bootstrapped splines, with the median of each measure reported. Hartigan & Hartigan's dip test for unimodality was used to determine the continuity of AmFRET values within the determined transition range. Plots are classified as "discontinuous" or "continuous" for p-values less than or greater than 0.05, respectively.

Plasmids that were determined to have a continuous transition were further classified as uniformly low ("low"), uniformly high ("high"), or transitioned from low to high with increasing concentration ("low to high"). This was done by extracting the minimum and ending AmFRET values from the spline fit. As a reference for the AmFRET value that indicates the start of a high FRET state, the AmFRET value of the transition start point of a control plasmid, rhx0927, was used. For each plasmid, if its minimum and ending AmFRET values fell below the reference, it was classified as low. If both fell above, it was classified as high. Those with a minimum value below and an ending value above were classified as "low to high". The majority classification of replicates for each plasmid is reported.

Calculating centrality measures

To determine betweenness and degree of centrality, we extracted interactions involving DFD-containing proteins (listed in **Table S1**) from STRING version 12.0,[122] considering only physical interactions with scores of 900 or higher. Using NetworkX v3.1, we analysed these interactions as an undirected graph to calculate betweenness and degree of centrality. For proteins with multiple DFDs, we classified a protein as discontinuous if any of its DFDs were identified as discontinuous.

Determination of positive nucleating interactions

We first excluded files with fewer than 2500 events positive for mEos3 or mean acceptor intensities less than 3.5 p.d.u. From this, any DFD or seed left with less than 25% of their

original instances after filtering were removed from the analysis completely. Next, we identified nucleating interactions as DFD pairs that decreased the C50 and increased the fraction assembled (fgate). We standardized all variables for each experimental batch of DFDs to a mean of 0 and variance of 1. We then determined the outlier degree for C50 and fgate based on the number of interquartile ranges below or above the median for these values. This was done directionally on a per-DFD basis. We defined the "nucleating interactions" for a given mEos3-fused DFD as those whose mean of these two values (reported as "seedability") is greater than or equal to 3 standard deviations above the mean of all seedability values. We confirmed that the seedability values for most DFD pairs partitioned with that of two negative controls included for each DFD.

To evaluate the reproducibility of our assay, we replicated it for a set of 36 DFDs. This replicate analysis mirrored the original, except it utilized the DFD distributions and cutoff values from the first set. The Pearson correlation (R) between the two sets was 0.91 ($p < 0.0001$). To minimize the impact of random variations in negatives and outliers, we excluded double negative instances, resulting in a slightly altered Pearson correlation (R) of 0.90 ($p < 0.0001$). Of the 3423 DFD + seed combinations reassessed, 16 showed inconsistent hit-calling, indicating an assay consistency rate of 99.53% with a 95% confidence interval ranging from 99.30% to 99.76%.

Approximating C_{sat} and supersaturability

To generate an average DAmFRET curve, we computed the mean of each histogram bin in the DAmFRET dataset, focusing on bins containing a minimum of 100 cells. The average DAmFRET curve for each DFD in the presence of its self-seed was fit to a Weibull function as follows. We first calculated the average AmFRET value in each concentration bin. The resulting curves resemble the fraction-assembled curves except that the asymptote is the maximum AmFRET value rather than 1. Therefore, we used the following equation for fitting:

$$\text{□□□□□□}(\text{□}) = \text{□□□}[1 - \text{□□□}(-\text{□□}(2)(\frac{\text{□}}{\text{□}50})^{\text{□}})] \text{ (Eq. 1)}$$

Here Amp is the AmFRET asymptotic value of the curve, c is the concentration, $C50_{seeded}$ is the concentration at which the curve, in the presence of its self-seed, has reached 50% of its asymptotic value, and □ describes the steepness of the stretched exponential. Initial values of the parameters were chosen based on Gaussian smoothed versions of the curves and constrained in the fit to at minimum a 2-fold change from those initial guesses. The □ parameter was constrained between 0.1 and 10 based on expected reasonable values of that parameter. At low and high concentration values, the average AmFRET values are clearly unstable and influenced by noise and minor compensation errors. Therefore, we chose the beginning and ending points of each curve by visual inspection, choosing starting points where the curve begins to increase and ending points where the curve levels off. Error values were determined from Monte Carlo simulations as in the fitting of fraction assembly.

To approximate the supersaturability of DFDs, we used the ratio of the average C50 in the presence of the respective DFD's seed ($C50_{seeded}$) to the average C50 in the presence of a null-seed ($C50_{stochastic}$). Ratios were only calculated between C50s obtained from the same batch run.

Cell culture

HEK293T cells and THP-1 cells were purchased from ATCC. THP-1 *PYCARD*-KO (thp-koascz) cells were purchased from InvivoGen. HEK293T cells were grown in Dulbecco's Modified Eagle's Medium (DMEM) with L-glutamine, 10% fetal bovine serum (FBS), and PenStrep 100 U/mL. THP-1 cells were grown in Roswell Park Memorial Institute (RPMI) medium 1640 with L-glutamine and 10% FBS. All cells were grown at 37°C in a 5% CO_2 atmosphere incubator. Cell lines were regularly tested for mycoplasma using the Universal mycoplasma detection kit (ATCC, #30-1012K).

Generation of stable cell lines

Stable cell lines were created as described.[12] Briefly, constructs were packaged into lentivirus in a 10 cm plate 60% confluent of HEK293T cells using the TransIT-LT1 (Mirus Bio, MIR2300) transfection reagent and 7 μg of the vector, 7 μg psPAX2, and 1 μg pVSV-G. Lentivirus was harvested and incubated with 293T with polybrene or infected at 1000x g for 1 h for THP-1 cells. For transduction of pCW57.1 derived vectors, HEK293T and THP-1 cells were selected with Puromycin (1 μg/mL) for 7 days. After this time, cells were sorted for positive expression of mScarlet-I and expanded in continuing selection with puromycin. For transduction of plasmids encoding fusions to miRFP670nano-Cryclust, THP-1 and HEK293T cells were selected with hygromycin B (350 μg/mL and 150 μg/mL, respectively) for 7 days. Cells were sorted for positive expression of miRFP670nano and expanded for further experiments with continued selection. To generate THP-1 PYCARD-KO + FADD-KO cells, sgRNA targeting FADD exon1 was cloned into the lentiCRISPR v2-Blast (Addgene #83480). This vector was packaged into lentivirus as described above. THP-1 PYCARD-KO cells were transduced using spinfection and supplemented with polybrene. 24 h after spinfection, media was replaced. 48 h after spinfection, cells were selected with blasticidin (1 μg/mL). After 10 days of blasticidin selection, single-cell clonal expansion was done by serial dilution of resistant cells to achieve complete knockouts. Selected wells were analysed by immunoblot to confirm the absence of FADD protein and sequence-verified.

High-content imaging analysis

High-content imaging was performed on the Opera Phenix high-content screening system (PerkinElmer) using a 63x water immersion objective. Briefly, yeast (rhy2977) transformed with individual plasmids were cultured and induced as for DAmFRET assays. Then, 10 μL were transferred into a well containing 90 μL of SGal-URA of a 96-well optically clear flat-bottom plate (PerkinElmer 6055302). Data analysis of the high content imaging was performed in Fiji. Images of mEos3 were acquired using 488 nm excitation and a standard GFP filter set. Small z-

stacks were acquired over 5 µm total range with 1 µm steps. The image containing the brightest mEos3 signal was used. The mEos3 signal was then background-subtracted with a rolling ball radius of 100 pixels then found and converted to Fiji ROIs using the Fiji Default method of traditional image thresholding. The mean, standard deviation, and aspect ratio (AR) were measured for each object. The coefficient of variation (CV) in pixel intensity was calculated for every object following the formula: CV = Std Dev/Mean*100. The wells were divided into 3 categories based on their AR and CV. Objects that had a CV > 55 and an AR > 1.159 were designated "fibrillar". Objects that had a CV > 55 and an AR < 1.16 were designated "punctate". Finally, objects that had a CV < 55 and an AR < 1.16 were designated "diffuse". These cutoffs were determined manually from a visual inspection of the data. Plasmids rhx4763 - rhx4767 were acquired in a second data set that used different laser powers and integration times. Hence, for these plasmids specifically, "fibrillar" had a CV > 17 and an AR > 1.4, "punctate" had a CV > 17 and an AR < 1.41, and "diffuse" had a CV < 18 and an AR < 1.41. These cutoffs were determined manually from a visual inspection of the data. The results were then manually verified for all wells. Seven plasmids were inconsistently classified by these cutoffs. Of these, manual inspection confirmed "diffuse" morphology for rhx1033 and rhx1133, and prompted reclassification of rhx2935, rhx2637, rhx1121, rhx1070, and rhx1055 from "fibrillar" to "punctate". Plasmid rhx2232 was incorrectly classified as punctate but images display fibrillar morphology. Three others (rhx1113, rhx1097, rhx2937) had anomalously high AR due to low expression. Representative microscopy images are included for all plasmids in our repository.

Fluorescence microscopy and optogenetic nucleation

The yeast and mammalian cells were imaged in an LSM 780 microscope with a 63x Plan-Apochromat (NA = 1.40) objective. T-Sapphire was excited with a 405 nm laser. mEos3 and mScarlet-I were excited with a 488 nm and 561 nm laser, respectively. For time-lapse imaging, samples were maintained at 37°C and 5% CO_2 with a stage top incubator. To stimulate Cry2clust we used the 488 nm laser at a power setting of 50% for a pulse of 10 s, which is the amount of time it took to scan the user-generated region of interest unless indicated otherwise. 561 and 633 nm lasers were used for imaging mScarlet-I and miRFP670nano, respectively. Pyroptosis events were tracked by incorporating the Sytox Orange reagent into the cell. To quantify the CV, images were subjected to an in-house Fiji adapted implementation of Cellpose for cellular segmentation.[123] The Cellpose-generated regions of interest (ROIs) were used to measure specified imaging channels.

For quantification of cell death events using IncuCyte (Sartorius), THP-1 cells were plated on a 24 or 96 well plate at a density of $4x10^8$/well or $1x10^8$/well, respectively, with PMA (10 ng/mL) for 16 h. Media was replaced with fresh media supplemented with Annexin V-Alexa488 and Sytox Orange (1:1000). For AIM2-Cry2clust activation, an initial collection of unexposed measurements was taken for 30 min. Then, the plate was exposed to 488 nm laser every 5 min. For treatments with poly(dA:dT), cells were treated and immediately subjected to imaging every

30 min for 19 h. Positive cells for either fluorophore were identified using the integrated software in the IncuCyte instrument.

For optogenetic activation of APAF1^{CARD} and NCLR4^{CARD}, HEK293T cells expressing lentivirus constructs were seeded on a 35-mm dish (ibidi) at a density of $4x10^4$/mL with 2 mL of media. The next day, dox was added at a concentration of 1 µg/mL to induce the expression of mScarlet-I tagged proteins. 24 h after protein induction, media was replaced with fresh media supplemented with Incucyte® Caspase-3/7 Dye (1:1000) 2 h prior to the experiment or Annexin V-Alexa488. Cells were imaged using a spinning-disk confocal microscope (Nikon, CSU-W1) with a ×60 Plan Apochromat objective (NA = 1.40) and a Flash 4 sCMOS camera (Hamamatsu). A region of interest (ROI) was selected to induce optogenetic activation for indicated times using a 488 nm laser at 50% laser power for the indicated time ranging from a fraction of a second to 30 s. ROIs were generated by Cellpose segmentation algorithm around each cell contour. These ROIs were then used to measure the area, mean, standard deviation, and integrated density of each cell on the 488 nm and 560 nm fluorescence channels.

Protein immunodetection

We performed capillary based protein immunodetection (Wes, ProteinSimple) as described.[12] Briefly, protein lysates were prepared as per recommended manufacturer instructions to a final concentration of 1 µg/mL. An assay plate was filled with samples, blocking reagent, primary antibodies (1:50 dilution for anti-Actin, 1:200 dilution for anti PYCARD), HRP-conjugated secondary antibodies and chemiluminescent substrate. The plate was subjected to electrophoretic protein separation and immunodetection in the fully automated capillary system. The rulting data was processed using the open-source software Compass (https://www.proteinsimple.com/compass/downloads/) to extract the intensities for the peaks corresponding to the expected molecular weight of proteins of interest. For western blot, cells were centrifuged at 1000 x g for 5 min and resuspended in lysis buffer (50 mM Tris (pH 7.4), 137 mM NaCl, 1 mM EDTA, 1% Triton X-100, 10 mM DTT (dithiothreitol), cOmplete Protease Inhibitor (1 tablet / 10 mL) (Roche, 11697498001). Protein lysates were resolved on a NuPAGE™ 4 to 12%, Bis-Tris gel and transferred onto a PVDF membrane (IPVH00010, Millipore) using the Pierce Power Blotter (ThermoFisher). The membrane was blocked with 5% skim milk and incubated overnight with the antibodies: anti-Actin (1:1000, sc-8432), anti-FADD (1:500, 05-486) and anti-PYCARD (1:1000, sc-514414). Primary antibody was removed by several washes with TBS + 0.1% Tween-20 and then subjected to incubation with secondary antibody (anti-mouse-HRP, 7076S, Cell Signaling Technology). The detection of protein bands was then carried out using enhanced chemiluminescence (ECL) (SuperSignal West Pico Chemiluminescent Substrate, ThermoFisher, 34577). The chemiluminescent signal was acquired by placing the membrane in a film cassette and exposing it to X-ray film (Kodak) at varying durations in a darkroom. After exposure, films were developed using an automatic film processor.

Semidenaturating Detergent-Agarose Gel Electrophoresis (SDD-AGE)

SDD-AGE was performed as previously described.[16] Briefly, cells were lysed using a 2010 Geno/Grinder with bead-beating. Samples were prepared with 2% sarkosyl and separated in a 1.5% agarose gel with 0.1% SDS. The distribution of mEos3-fused proteins was analysed directly in the gel with a GE Typhoon Imaging System. Images were processed to remove background using a 250-pixel rolling ball, cropped, and contrast-adjusted.

Quantification and statistical analysis

Two-sided Student's t-tests were used for significance testing unless stated otherwise for two sample comparisons. The graphs represent the means ± SEM of independent biological experiments unless stated otherwise. Statistical analysis was performed using GraphPad Prism 9, Python and R packages.

Supplementary figure legends

Figure S1. **Sequence, imaging and DAmFRET analysis reveal diverse sequence-encoded phase behaviours of DFDs, related to Figure 1**

A. Schematic diagram of all DFDs characterized in this paper, and their classification into structural subfamilies. Tandem DFDs are highlighted in red, but were analysed with their corresponding single DFD subfamilies.
B. Matrices of predicted alignment error (PAE) for the indicated regions of proteins containing two DFDs, as reported in the AlphaFold Protein Structure Database,[120] grouped into two categories according to interdomain PAE values consistent with either independent (left) or dependent (right) relative geometries of the DFDs.
C. DAmFRET profiles of representative DFDs classified as continuous or discontinuous.
D. Classification of continuous DFD as “low”, “low to high”, or “high” by thresholding on the minimum and ending AmFRET values of a fitted spline, normalized to that of a control DFD.
E. Classification of the proteins as entirely diffuse, fibrillar or punctate based on boundaries on the scatter plot of coefficient of variation vs aspect ratio. The colored circles represent the mean and covariance of the values for each category.
F. Images of yeast expressing representative DFDs, in the absence of seeds, classified as fibrillar that produced continuous (low to high) DAmFRET profiles. Scale bar 10 µm.
G. Images of yeast expressing representative DFDs, in the absence of seeds, classified as fibrillar that produced discontinuous DAmFRET profiles. Scale bar 10 µm.
H. Images of yeast expressing representative DFDs, in the absence of seeds, classified as punctate that produced continuous (low to high) DAmFRET profiles. Scale bar 10 µm.
I. Representative confocal microscopy images of yeast expressing the indicated DFD constructs in the presence of ASC^{FL} or $CARD14^{CARD}$ seeds. The images show the emergence of filaments only from µNS seeds containing the matching DFD.

Figure S2. **Self-assembly involves subunit interfaces shared with solved DFD polymer structures, related to Figure 1**

A. Representative DAmFRET plots for the indicated DFDs with the indicated point mutations. The horizontal line approximates the mean AmFRET value for monomeric mEos3. Procedure defined units (p.d.u.).
B. Image of SDD-AGE showing the size distribution of detergent-resistant multimers (where present) of mEos3-fused proteins expressed in yeast. The amyloid-forming protein, $RIPK1^{RHIM}$, formed detergent-resistant multimers whereas all DFD multimers were detergent-labile.

Figure S3. **Proteins with DFDs that have seedable and/or discontinuous DAmFRET are central to their physical interaction networks and are more likely to be supersaturated in vivo, related to Figure 2**

A. Transcripts encoding proteins with discontinuous DFDs have higher expression in immune cells. P values are from Mann-Whitney test (see also Table S5). Transcripts per million (TPM) values are from the immune cell data of the Human Protein Atlas, comprising 18 cell types and total Peripheral Blood Mononuclear Cells (PBMC).
B. Heatmap of protein abundance relative to reference, of discontinuous and continuous DFD containing proteins for the indicated tissues. Tissues are ordered by significance. P values are from Mann-Whitney test (see also Table S5). Protein abundance values are from the Proteome Map of the Human Body.[30]
C. Bar plot of the Spearman R correlation between immune cell type transcript abundance and C_{sat} values of DFDs shows consistent negative and significant anticorrelation among immune cell types. Data were obtained from the immune cell section of the Human Protein Atlas.
D. Boxplot comparing the betweenness (left) and degree centrality (right) of DFD-containing proteins that are either non-seedable or continuous (n = 37) to those that are both seedable and discontinuous (n = 14). Seedable, discontinuous proteins were found to have a significantly higher betweenness and degree centrality than non-seedable or continuous proteins. Mann-Whitney U = 145.5 (p = 0.012) and U = 146.5 (p = 0.017), respectively.
E. Permutation test (n = 10000) comparing betweenness centrality (top) and degree centrality (bottom) for continuous and discontinuous DFDs. Mann-Whitney U = 274 (p = 0.028) and 242 (p = 0.008), respectively.
F. Boxplot comparing the betweenness (left) and degree centrality of Sterile Alpha Motif (SAM) containing proteins network with continuous and discontinuous DFD networks. SAM containing protein network was extracted from STRING version 12.0 physical interaction database with a score higher than 900. Mann-Whitney U = 34 ($p < 0.001$) and U = 145 (p = 0.799), respectively between SAM (n=17) and discontinuous DFD (n=18).

Figure S4. **Proteins characterized as signaling adaptors display discontinuity in its DFD and FL context, related to Figure 2**

A. Pairs of DAmFRET plots comparing the behaviours of representative DFDs and their corresponding FL proteins. Dashed horizontal lines approximate the mean AmFRET value for monomeric mEos3. FL MAVS has appreciable AmFRET in the supersaturated state that we attribute to its mitochondrial localization signal.
B. Left, DAmFRET plot of ASC^{PYD} expressed alone. Right, DAmFRET plot of ASC^{PYD} co-expressed with FL NLRP3 showing persistence of the supersaturated bottom population indicating that FL NLRP3 oligomers are not active (in the absence of stimulation).

Figure S5. **Full length proteins displaying discontinuous profiles can be self-seeded, related to Figures 1 and 2**

A. Representative DAmFRET plots for the indicated full length proteins. Seeds comprised μNS-mCardinal fusion proteins either lacking (left) or containing (right) the corresponding DFD. The horizontal dotted lines approximate the mean AmFRET value for monomeric mEos3.

Figure S6. **Characterization of engineered THP-1 cell lines and apoptosome assembly, and correlation of DFD supersaturation with cell mortality in the human body, related to Figures 3 and 4**

A. DAmFRET plots of $APAF1^{CARD}$ and $CASP9^{CARD}$ measured in the presence of the indicated "seeds" expressed in trans. Both proteins fail to populate a high-AmFRET state.
B. Western blot verifying the knock-out status of ASC and/or FADD in the respective engineered stable THP-1 cell lines. Actin is the loading control.
C. Cartoon depicting the doxycycline-inducible ASC-mScarlet-I that replaced endogenous ASC in THP-1 *PYCARD-KO* cells.
D. Representative capillary western blots comparing expression levels of the dox-inducible ASC-mScarlet-I construct alongside endogenous ASC. Actin is the loading control.
E. Quantification of the data showing significantly lower-than endogenous levels of ASC in the engineered construct at even the highest level of induction by doxycycline. For each condition, one million cells were sorted and lysed.
F. Scatter plot showing the relationship between ASC supersaturation (as approximated by the ratio of transcription levels and C_{sat} values) and mean lifespan for each cell type as indicated in Figure 4H. The red line represents the best-fit power-law regression, obtained by performing linear regression in log-log space. The shaded region represents the 95% confidence interval for the trend line. Spearman R = -0.87 (two-tailed p = 0.0000057).
G. Bar plot of the Spearman R correlation between supersaturation and cell mean lifespan of cell types as shown in Figure 4H for each DFD. Transcript levels for each cell type were obtained from the single cell RNA dataset of the Human Protein Atlas.

Figure S7. **Generation and validation of the DFD nucleating interactome, related to Figure 5**

A. Illustration of how the library of all pairs of DFDs was created. An arrayed sublibrary of yeast transformed with 105 DFD-mEos3 fusions was mated to a separate arrayed sublibrary of yeast strains expressing 107 chromosomally integrated DFD-μNS-mCardinal fusions, to create a library of 12,660 diploid strains representing all pairwise combinations.

B. Left, DAmFRET was run on all pairwise combinations. Only high quality datasets -- having a total cell count greater or equal to 2500 and a mean acceptor intensity greater or equal to 3.5 p.d.u. -- were used in the analysis. Right, DAmFRET plots of $FADD^{FL}$ either null-seeded (lacking a DFD) or self-seeded. Nucleating interactions (as shown by the self-seeded example) are indicated by a reduced C50 and increased percentage of cells with self-assemblies (those above the gate delimiting low FRET, shown in orange).

C. Hits are determined by a multiparameter combination of the degree of C50 outlier and the degree of fraction assembled outlier as defined by how many interquartile ranges (IQR) a plot is below or above the median, respectively. Points on the graph are shaded by this parameter. The leftmost set of boxplots show the distribution of standardized log10 C50 and fraction assembled for all seeds for a representative protein, $FADD^{FL}$. The middle boxplot shows the average outlier degree value of these two parameters. This value is referred to as "seedability" throughout the text and is used in determining hits. The cutoff value for hit determination was set to be 3 standard deviations above the mean of all seedability values across the screen. The scatter plot on the right shows the standardized log10 C50 and fraction assembled values, depicting the contribution of both to the scoring value and positive nucleating interactions within the green box.

D. Top, scatter plot of seedability values from the two replicate experiments containing 3478 DFD + seed combinations. Points are colored according to agreement between the two experiments. Gray rectangles indicate seedability values of negative interactions, with the dark gray square containing the interaction found to be negative for both instances. Bottom, the replicates after the removal of instances found to be negative in both experiments to reduce random and outlier effects. The line of best fit is shown in red. Pearson correlation R between the two experiments = 0.91 ($p < 0.0001$). In order to reduce the effects of random variations of the negatives as well as outlier effects, we omitted double negative instances. In this case, the Pearson correlation R = 0.90 ($p < 0.0001$).

E. Seventeen DFD + seed combinations that had inconsistent hit-calling out of the 3478 combinations reassessed. From this we determine that our assay had a consistency of 99.51% with a 95% confidence interval of 99.28 - 99.74%.

F. Bar plots showing the number of hits per experiment, as well as total number of hits, determined for each replicated DFD. Blue and yellow indicate separate hit counts for each experiment. Gray are the number of unique hits found across both experiments. What percentage of seeds are consistently called hits are shown for each DFD. The left bar plot shows the overall summary of all DFDs included in both sets.

Figure S8. Demonstration of conserved energy storage capacity of DFDs, related to Figure 6

A. DAmFRET data of DFD-only and full length inferred DISC components from the model sponge, *Amphimedon queenslandica*. The distant homolog to human FADD exhibits supersaturability in its FL and isolated DFDs.
B. DAmFRET data of DFD-only and full length inflammasome components from the model fish *Danio rerio*.

Supplementary Materials

Supplementary text. **Experiments to investigate the nature of DFD assembly.** DAmFRET data do not clarify if self-assembly involves native DFD interactions rather than amyloid-like misfolding.[16] To address this question, we introduced point mutations to disrupt assembly via conserved known interfaces between folded DFD subunits.[23,37] Across the multiple DFDs examined, all such mutations indeed reduced or eliminated the high-AmFRET population (**Figure S2A**). To directly evaluate the nature of DFD assembly in our experiments, we subjected the seeded and unseeded cells to semi-denaturing detergent-agarose gel electrophoresis (SDD-AGE), a technique that distinguishes amyloids from other protein states based on their detergent-resistance and size dispersity.[124] We found that unlike our amyloid control ($RIPK1^{RHIM}$), none of the DFD assemblies survived sarkosyl exposure (**Figure S2B**), consistent with their retaining the death fold rather than misfolding into amyloid. Ongoing work is elucidating the physical basis of these nucleation barriers.

Table S1. **Metadata, construct specifics, and data for the human DFDs analysed in this study, related to Figures 1 and 2.** ND (not determined). NA (not applicable/available). FL (full-length). [a]rhx1073b, rhx1102b, rhx1108, and rhx1135 did not have a majority automated classification and were therefore classified by manual inspection. [b]Inspection of the DAmFRET plots of the six nonseedable discontinuous DFDs reveal that most are only slightly discontinuous, and include $CARD9^{CARD}$ which we previously showed to have a negligible nucleation barrier,[37] indicating that at least some of these six are misclassified due to heterogeneity between cells around C_{sat}.

Table S2. **Metadata, construct specifics, and data for additional proteins analysed in this study, related to Figure 2.** FL (full-length). [a]Mutations were made to inactivate enzymatic activity for cell death effectors.

Table S3. **Specifics of lentivirus vectors used in this study, related to Figures 4 and 5.**

Table S4. **Nucleating interactome of DFDs, related to Figure 5.** Note that plasmids rhx2938, rhx1071, rhx2934, rhx1113, rhx1064, rhx2933, and rhx1368; and seeds from rhx2938, rhx2933 and rhx2934; did not pass quality control as outlined in methods and were therefore omitted from the analysis.

Table S5. **Transcript and protein abundance statistics, related to Figure S3.**

Movie S1. **Time-lapse movie of cells expressing opto-APAF1 (top) and CASP9-mScarlet-I (bottom) showing one minute of blue light induction and subsequent recovery, related to Figure 3.** Non-supersaturable opto-APAF1 allows clusters to dissolve following stimulation. Scaler bar 10 µm.

Movie S2. **Time-lapse movie of cells expressing opto-NLRC4 (top) and**

CASP9(CASP1^{CARD})-mScarlet-I (bottom), showing one minute of blue light induction and subsequent recovery, related to Figure 3. Supersaturable opto-NLRC4 continues to drive cluster growth following stimulation. Scaler bar 10 µm.

Movie S3. **Time-lapse movie of cells expressing opto-AIM2, following 10 seconds of blue light induction, related to Figure 4.** Left panel: opto-AIM2. Middle panel: Sytox Orange fluorescence. Right panel: Bright field. Following 10 seconds of blue light induction, opto-AIM2 clusters form, leading to cell death (Sytox Orange uptake). Scale bar: 10 µm.

Movie S4. **Time-lapse movie of cells expressing opto-AIM2(F27G), following 10 seconds of blue light induction, related to Figure 4.** Left panel: opto-AIM2(F27G). Middle panel: Sytox Orange fluorescence. Right panel: Bright field. Following 10 seconds of blue light induction, opto-AIM2(F27G) clusters form and rapidly dissociate, failing to induce cell death. Scale bar: 10 µm.

Acknowledgements

We thank Nick Grishin and Lisa Kinch for creating structure-guided alignments of DFDs early in this work, and Mark Miller for assistance with illustrations. This work was performed to fulfill, in part, requirements for ARG's thesis research in the Graduate School of the Stowers Institute for Medical Research. This work was supported by the National Institute of General Medical Sciences (Award Number R01GM130927, to RH) and the National Institute on Aging (Award Number F99AG068511, to ARG) of the National Institutes of Health, the American Cancer Society (RSG-19-217-01-CCG to RH), and the Stowers Institute for Medical Research. The funders had no role in study design, data collection and analysis, or manuscript preparation. The content is solely the responsibility of the authors and does not necessarily represent the official views of the funders.

Author Contributions

Conceptualization, A.R.G., S.V., and R.H.; Methodology, A.R.G., T.M., S.V., J.J.L., J.R.U. and R.H.; Formal Analysis, A.R.G., T.M., J.J.L. and J.R.U.; Investigation, A.R.G., T.M., S.V., J.J.L., J.W., X.S., and D.B.; Writing – Original Draft, A.R.G. and R.H.; Writing – Review & Editing, A.R.G., S.V., T.M. and R.H.; Funding Acquisition, A.R.G. and R.H.; Supervision, R.H.

Declaration of Interests

The authors declare no competing interests.

Data availability

All DAmFRET and representative microscopy data can be accessed interactively on a dedicated website https://simrcompbio.shinyapps.io/HalfmannLab-Nucleating_Interactome/. Original data

underlying this manuscript can be accessed from the Stowers Original Data Repository at http://www.stowers.org/research/publications/libpb-2387

Bibliography

1. Mehta, P., Lang, A. H. & Schwab, D. J. Landauer in the age of synthetic biology: energy consumption and information processing in biochemical networks. *J. Stat. Phys.* **162**, 1153–1166 (2016).
2. Bérut, A. *et al.* Experimental verification of Landauer's principle linking information and thermodynamics. *Nature* **483**, 187–189 (2012).
3. Goldbeter, A. & Koshland, D. E. An amplified sensitivity arising from covalent modification in biological systems. *Proc Natl Acad Sci USA* **78**, 6840–6844 (1981).
4. Kagan, J. C., Magupalli, V. G. & Wu, H. SMOCs: supramolecular organizing centres that control innate immunity. *Nat. Rev. Immunol.* **14**, 821–826 (2014).
5. Aravind, L., Nicastro, G. G., Iyer, L. M. & Burroughs, A. M. The prokaryotic roots of eukaryotic immune systems. *Annu. Rev. Genet.* **58**, 365–389 (2024).
6. Wu, E. J. *et al.* A structural atlas of death domain fold proteins reveals their versatile roles in biology and function. *Proc Natl Acad Sci USA* **122**, e2426986122 (2025).
7. Wu, H. Higher-order assemblies in a new paradigm of signal transduction. *Cell* **153**, 287–292 (2013).
8. Kobe, B. *et al.* Signalling by co-operative higher-order assembly formation: linking evidence at molecular and cellular levels. *Biochem. J.* **482**, 275–294 (2025).
9. Huoh, Y.-S. & Hur, S. Death domain fold proteins in immune signaling and transcriptional regulation. *FEBS J.* **289**, 4082–4097 (2022).
10. Seyrek, K. *et al.* Controlling Cell Death through Post-translational Modifications of DED Proteins. *Trends Cell Biol.* **30**, 354–369 (2020).
11. Zheng, D., Liwinski, T. & Elinav, E. Inflammasome activation and regulation: toward a better understanding of complex mechanisms. *Cell Discov.* **6**, 36 (2020).

12. Rodriguez Gama, A., Miller, T., Lange, J. J., Unruh, J. R. & Halfmann, R. A nucleation barrier spring-loads the CBM signalosome for binary activation. *eLife* **11**, (2022).

13. Ioan Sarbu & Calin Sebarchievici. A comprehensive review of thermal energy storage. *Sustainability* **10**, 191 (2018).

14. Song, P. *et al.* Heat transfer and thermoregulation within single cells revealed by transient plasmonic imaging. *Chem* **7**, 1569–1587 (2021).

15. Thaker, S. K., Ch'ng, J. & Christofk, H. R. Viral hijacking of cellular metabolism. *BMC Biol.* **17**, 59 (2019).

16. Khan, T. *et al.* Quantifying nucleation in vivo reveals the physical basis of prion-like phase behavior. *Mol. Cell* **71**, 155-168.e7 (2018).

17. Jang, T. *et al.* Structural study of the RIPoptosome core reveals a helical assembly for kinase recruitment. *Biochemistry* **53**, 5424–5431 (2014).

18. Fosuah, E. *et al.* Assembly and activation of the death-inducing signaling complex. *Proc Natl Acad Sci USA* **122**, e2504819122 (2025).

19. Wang, L. *et al.* The Fas-FADD death domain complex structure reveals the basis of DISC assembly and disease mutations. *Nat. Struct. Mol. Biol.* **17**, 1324–1329 (2010).

20. Kandola, T. *et al.* Pathologic polyglutamine aggregation begins with a self-poisoning polymer crystal. *eLife* **12**, (2023).

21. Buell, A. K. The Nucleation of Protein Aggregates - From Crystals to Amyloid Fibrils. *Int. Rev. Cell Mol. Biol.* **329**, 187–226 (2017).

22. Lin, S.-C., Lo, Y.-C. & Wu, H. Helical assembly in the MyD88-IRAK4-IRAK2 complex in TLR/IL-1R signalling. *Nature* **465**, 885–890 (2010).

23. Lu, A. *et al.* Unified polymerization mechanism for the assembly of ASC-dependent

inflammasomes. *Cell* **156**, 1193–1206 (2014).

24. Rodríguez Gama, A., Miller, T. & Halfmann, R. Mechanics of a molecular mousetrap-nucleation-limited innate immune signaling. *Biophys. J.* **120**, 1150–1160 (2021).

25. Shearwin-Whyatt, L. M., Harvey, N. L. & Kumar, S. Subcellular localization and CARD-dependent oligomerization of the death adaptor RAIDD. *Cell Death Differ.* **7**, 155–165 (2000).

26. Posey, A. E. *et al.* Mechanistic inferences from analysis of measurements of protein phase transitions in live cells. *J. Mol. Biol.* **433**, 166848 (2021).

27. Kar, M. *et al.* Phase-separating RNA-binding proteins form heterogeneous distributions of clusters in subsaturated solutions. *Proc Natl Acad Sci USA* **119**, e2202222119 (2022).

28. Wang, M., Herrmann, C. J., Simonovic, M., Szklarczyk, D. & von Mering, C. Version 4.0 of PaxDb: Protein abundance data, integrated across model organisms, tissues, and cell-lines. *Proteomics* **15**, 3163–3168 (2015).

29. Karlsson, M. *et al.* A single-cell type transcriptomics map of human tissues. *Sci. Adv.* **7**, (2021).

30. Jiang, L. *et al.* A quantitative proteome map of the human body. *Cell* **183**, 269-283.e19 (2020).

31. Uhlen, M. *et al.* A genome-wide transcriptomic analysis of protein-coding genes in human blood cells. *Science* **366**, (2019).

32. Vecchi, G. *et al.* Proteome-wide observation of the phenomenon of life on the edge of solubility. *Proc Natl Acad Sci USA* **117**, 1015–1020 (2020).

33. Cai, X. *et al.* Prion-like polymerization underlies signal transduction in antiviral immune defense and inflammasome activation. *Cell* **156**, 1207–1222 (2014).

34. Bienz, M. Head-to-tail polymerization in the assembly of biomolecular condensates. *Cell* **182**, 799–811 (2020).

35. Qiao, F. & Bowie, J. U. The many faces of SAM. *Sci. STKE* **2005**, re7 (2005).

36. Knight, M. J., Leettola, C., Gingery, M., Li, H. & Bowie, J. U. A human sterile alpha motif domain polymerizome. *Protein Sci.* **20**, 1697–1706 (2011).

37. Holliday, M. J. *et al.* Structures of autoinhibited and polymerized forms of CARD9 reveal mechanisms of CARD9 and CARD11 activation. *Nat. Commun.* **10**, 3070 (2019).

38. Ohto, U. *et al.* Structural basis for the oligomerization-mediated regulation of NLRP3 inflammasome activation. *Proc Natl Acad Sci USA* **119**, e2121353119 (2022).

39. Hochheiser, I. V. *et al.* Structure of the NLRP3 decamer bound to the cytokine release inhibitor CRID3. *Nature* **604**, 184–189 (2022).

40. Sommer, K. *et al.* Phosphorylation of the CARMA1 linker controls NF-kappaB activation. *Immunity* **23**, 561–574 (2005).

41. Andreeva, L. *et al.* NLRP3 cages revealed by full-length mouse NLRP3 structure control pathway activation. *Cell* **184**, 6299-6312.e22 (2021).

42. Chuenchor, W., Jin, T., Ravilious, G. & Xiao, T. S. Structures of pattern recognition receptors reveal molecular mechanisms of autoinhibition, ligand recognition and oligomerization. *Curr. Opin. Immunol.* **26**, 14–20 (2014).

43. Green, D. R. Caspase activation and inhibition. *Cold Spring Harb. Perspect. Biol.* **14**, (2022).

44. Martinon, F., Burns, K. & Tschopp, J. The inflammasome: a molecular platform triggering activation of inflammatory caspases and processing of proIL-beta. *Mol. Cell* **10**, 417–426 (2002).

45. Seth, R. B., Sun, L., Ea, C.-K. & Chen, Z. J. Identification and characterization of MAVS, a mitochondrial antiviral signaling protein that activates NF-kappaB and IRF 3. *Cell* **122**, 669–682 (2005).

46. Kawai, T. *et al.* IPS-1, an adaptor triggering RIG-I- and Mda5-mediated type I interferon induction. *Nat. Immunol.* **6**, 981–988 (2005).

47. Micheau, O. & Tschopp, J. Induction of TNF receptor I-mediated apoptosis via two sequential signaling complexes. *Cell* **114**, 181–190 (2003).

48. Gross, O. *et al.* Card9 controls a non-TLR signalling pathway for innate anti-fungal immunity. *Nature* **442**, 651–656 (2006).

49. Bertin, J. *et al.* CARD9 is a novel caspase recruitment domain-containing protein that interacts with BCL10/CLAP and activates NF-kappa B. *J. Biol. Chem.* **275**, 41082–41086 (2000).

50. Bertin, J. *et al.* CARD11 and CARD14 are novel caspase recruitment domain (CARD)/membrane-associated guanylate kinase (MAGUK) family members that interact with BCL10 and activate NF-kappa B. *J. Biol. Chem.* **276**, 11877–11882 (2001).

51. Henry, C. M. & Martin, S. J. Caspase-8 Acts in a Non-enzymatic Role as a Scaffold for Assembly of a Pro-inflammatory “FADDosome” Complex upon TRAIL Stimulation. *Mol. Cell* **65**, 715-729.e5 (2017).

52. Tummers, B. *et al.* Caspase-8-Dependent Inflammatory Responses Are Controlled by Its Adaptor, FADD, and Necroptosis. *Immunity* **52**, 994-1006.e8 (2020).

53. Chen, G. *et al.* Phosphorylated FADD induces NF-kappaB, perturbs cell cycle, and is associated with poor outcome in lung adenocarcinomas. *Proc Natl Acad Sci USA* **102**, 12507–12512 (2005).

54. Gurung, P. *et al*. FADD and caspase-8 mediate priming and activation of the canonical and noncanonical Nlrp3 inflammasomes. *J. Immunol.* **192**, 1835–1846 (2014).

55. Mouasni, S. & Tourneur, L. FADD at the Crossroads between Cancer and Inflammation. *Trends Immunol.* **39**, 1036–1053 (2018).

56. Balachandran, S., Thomas, E. & Barber, G. N. A FADD-dependent innate immune mechanism in mammalian cells. *Nature* **432**, 401–405 (2004).

57. Li, P. *et al.* Cytochrome c and dATP-dependent formation of Apaf-1/caspase-9 complex initiates an apoptotic protease cascade. *Cell* **91**, 479–489 (1997).

58. Tinel, A. & Tschopp, J. The PIDDosome, a protein complex implicated in activation of caspase-2 in response to genotoxic stress. *Science* **304**, 843–846 (2004).

59. Headon, D. J. *et al.* Gene defect in ectodermal dysplasia implicates a death domain adapter in development. *Nature* **414**, 913–916 (2001).

60. Gong, Y.-N., Crawford, J. C., Heckmann, B. L. & Green, D. R. To the edge of cell death and back. *FEBS J.* **286**, 430–440 (2019).

61. Nano, M., Mondo, J. A., Harwood, J., Balasanyan, V. & Montell, D. J. Cell survival following direct executioner-caspase activation. *Proc Natl Acad Sci USA* **120**, e2216531120 (2023).

62. Häcker, G. & Haimovici, A. Sub-lethal signals in the mitochondrial apoptosis apparatus: pernicious by-product or physiological event? *Cell Death Differ*. **30**, 250–257 (2023).

63. Park, H. *et al.* Optogenetic protein clustering through fluorescent protein tagging and extension of CRY2. *Nat. Commun.* **8**, 30 (2017).

64. Shkarina, K. *et al.* Optogenetic activators of apoptosis, necroptosis, and pyroptosis. *J. Cell Biol.* **221**, (2022).

65. Kennedy, M. J. *et al.* Rapid blue-light-mediated induction of protein interactions in living cells. *Nat. Methods* **7**, 973–975 (2010).

66. Lee, S. *et al.* AIM2 forms a complex with pyrin and ZBP1 to drive PANoptosis and host defence. *Nature* **597**, 415–419 (2021).

67. Maelfait, J., Liverpool, L. & Rehwinkel, J. Nucleic acid sensors and programmed cell death. *J. Mol. Biol.* **432**, 552–568 (2020).

68. Place, D. E. *et al.* Hierarchical Cell Death Program Disrupts the Intracellular Niche Required for Burkholderia thailandensis Pathogenesis. *MBio* **12**, e0105921 (2021).

69. Roncaioli, J. L. *et al.* A hierarchy of cell death pathways confers layered resistance to shigellosis in mice. *eLife* **12**, (2023).

70. Bindels, D. S. *et al.* mScarlet: a bright monomeric red fluorescent protein for cellular imaging. *Nat. Methods* **14**, 53–56 (2017).

71. Che, D. L., Duan, L., Zhang, K. & Cui, B. The Dual Characteristics of Light-Induced Cryptochrome 2, Homo-oligomerization and Heterodimerization, for Optogenetic Manipulation in Mammalian Cells. *ACS Synth. Biol.* **4**, 1124–1135 (2015).

72. He, W. *et al.* Gasdermin D is an executor of pyroptosis and required for interleukin-1β secretion. *Cell Res.* **25**, 1285–1298 (2015).

73. Sender, R. & Milo, R. The distribution of cellular turnover in the human body. *Nat. Med.* **27**, 45–48 (2021).

74. Bedoui, S., Herold, M. J. & Strasser, A. Emerging connectivity of programmed cell death pathways and its physiological implications. *Nat. Rev. Mol. Cell Biol.* **21**, 678–695 (2020).

75. Gullett, J. M., Tweedell, R. E. & Kanneganti, T.-D. It's All in the PAN: Crosstalk, Plasticity, Redundancies, Switches, and Interconnectedness Encompassed by PANoptosis

Underlying the Totality of Cell Death-Associated Biological Effects. *Cells* **11**, (2022).

76. Park, H. H. *et al.* The death domain superfamily in intracellular signaling of apoptosis and inflammation. *Annu. Rev. Immunol.* **25**, 561–586 (2007).

77. Unable to find information for 14887333.

78. Kibby, E. M. *et al.* Bacterial NLR-related proteins protect against phage. *Cell* **186**, 2410-2424.e18 (2023).

79. Yuen, B., Bayes, J. M. & Degnan, S. M. The characterization of sponge NLRs provides insight into the origin and evolution of this innate immune gene family in animals. *Mol. Biol. Evol.* **31**, 106–120 (2014).

80. Sakamaki, K. *et al.* The apoptotic initiator caspase-8: its functional ubiquity and genetic diversity during animal evolution. *Mol. Biol. Evol.* **31**, 3282–3301 (2014).

81. Ferrao, R. & Wu, H. Helical assembly in the death domain (DD) superfamily. *Curr. Opin. Struct. Biol.* **22**, 241–247 (2012).

82. Fu, T.-M. *et al.* Cryo-EM Structure of Caspase-8 Tandem DED Filament Reveals Assembly and Regulation Mechanisms of the Death-Inducing Signaling Complex. *Mol. Cell* **64**, 236–250 (2016).

83. Wu, S. *et al.* Design principles for inflammasome inhibition by pyrin-only-proteins. *eLife* **13**, (2024).

84. Lu, A. *et al.* Molecular basis of caspase-1 polymerization and its inhibition by a new capping mechanism. *Nat. Struct. Mol. Biol.* **23**, 416–425 (2016).

85. de Almeida, L. *et al.* The PYRIN Domain-only Protein POP1 Inhibits Inflammasome Assembly and Ameliorates Inflammatory Disease. *Immunity* **43**, 264–276 (2015).

86. Jeong, H., Mason, S. P., Barabási, A. L. & Oltvai, Z. N. Lethality and centrality in protein

networks. *Nature* **411**, 41–42 (2001).

87. Nithya, C., Kiran, M. & Nagarajaram, H. A. Dissection of hubs and bottlenecks in a Protein-protein Interaction Network. *Comput. Biol. Chem.* 107802 (2022) doi:10.1016/j.compbiolchem.2022.107802.

88. Pang, E., Hao, Y., Sun, Y. & Lin, K. Differential variation patterns between hubs and bottlenecks in human protein-protein interaction networks. *BMC Evol. Biol.* **16**, 260 (2016).

89. Schleker, S. & Trilling, M. Data-warehousing of protein-protein interactions indicates that pathogens preferentially target hub and bottleneck proteins. *Front. Microbiol.* **4**, 51 (2013).

90. Lannoy, V., Côté-Biron, A., Asselin, C. & Rivard, N. TIRAP, TRAM, and Toll-Like Receptors: The Untold Story. *Mediators Inflamm.* **2023**, 2899271 (2023).

91. Ve, T. *et al.* Structural basis of TIR-domain-assembly formation in MAL- and MyD88-dependent TLR4 signaling. *Nat. Struct. Mol. Biol.* **24**, 743–751 (2017).

92. Chen, X. *et al.* Mosaic composition of RIP1-RIP3 signalling hub and its role in regulating cell death. *Nat. Cell Biol.* **24**, 471–482 (2022).

93. Moncrieffe, M. C. *et al.* MyD88 Death-Domain Oligomerization Determines Myddosome Architecture: Implications for Toll-like Receptor Signaling. *Structure* **28**, 281-289.e3 (2020).

94. Cao, F., Deliz-Aguirre, R., Gerpott, F. H., Ziska, E. & Taylor, M. J. Myddosome clustering in IL-1 receptor signaling regulates the formation of an NF-kB activating signalosome. *EMBO Rep.* **24**, e57233 (2023).

95. Fisch, D. *et al.* Molecular definition of the endogenous Toll-like receptor signalling

pathways. *Nature* **631**, 635–644 (2024).

96. O'Carroll, A. *et al.* Pathological mutations differentially affect the self-assembly and polymerisation of the innate immune system signalling adaptor molecule MyD88. *BMC Biol.* **16**, 149 (2018).

97. Deliz-Aguirre, R. *et al.* MyD88 oligomer size functions as a physical threshold to trigger IL1R Myddosome signaling. *J. Cell Biol.* **220**, (2021).

98. Lizana, J., Sanchez-Jimenez, P. E., Chacartegui, R., Becerra, J. A. & Perez-Maqueda, L. A. Supercooled sodium acetate aqueous solution for long-term heat storage to support heating decarbonisation. *Journal of Energy Storage* **55**, 105584 (2022).

99. Sharma, A., Tyagi, V. V., Chen, C. R. & Buddhi, D. Review on thermal energy storage with phase change materials and applications. *Renew. Sustain. Energy Rev* **13**, 318–345 (2009).

100. Shen, C. *et al.* Phase separation drives RNA virus-induced activation of the NLRP6 inflammasome. *Cell* **184**, 5759-5774.e20 (2021).

101. Liu, D. *et al.* IFI16 phase separation via multi-phosphorylation drives innate immune signaling. *Nucleic Acids Res.* **51**, 6819–6840 (2023).

102. Vekilov, P. G. Phase diagrams and kinetics of phase transitions in protein solutions. *J. Phys. Condens. Matter* **24**, 193101 (2012).

103. Martin, E. W. *et al.* A multi-step nucleation process determines the kinetics of prion-like domain phase separation. *Nat. Commun.* **12**, 4513 (2021).

104. Shimobayashi, S. F., Ronceray, P., Sanders, D. W., Haataja, M. P. & Brangwynne, C. P. Nucleation landscape of biomolecular condensates. *Nature* **599**, 503–506 (2021).

105. Salvesen, G. S. & Dixit, V. M. Caspase activation: the induced-proximity model. *Proc*

Natl Acad Sci USA **96**, 10964–10967 (1999).

106. Lichtenstein, M. A. *et al*. Bottom-up reconstruction of functional death fold signalosomes reveals a requirement for polymer stability and avidity. *Science* **388**, 415–422 (2025).

107. Heo, T. W. & Chen, L.-Q. Phase-Field Modeling of Nucleation in Solid-State Phase Transformations. *JOM* **66**, 1520–1528 (2014).

108. Barton, J. P. & Sontag, E. D. The energy costs of insulators in biochemical networks. *Biophys. J.* **104**, 1380–1390 (2013).

109. Capra, E. J., Perchuk, B. S., Skerker, J. M. & Laub, M. T. Adaptive mutations that prevent crosstalk enable the expansion of paralogous signaling protein families. *Cell* **150**, 222–232 (2012).

110. Zarrinpar, A., Park, S.-H. & Lim, W. A. Optimization of specificity in a cellular protein interaction network by negative selection. *Nature* **426**, 676–680 (2003).

111. Garg, A. *et al.* Structural insights into the atypical filament assembly of pyrin domain-containing IFI16. *EMBO J.* (2025) doi:10.1038/s44318-025-00626-7.

112. Park, H. H. *et al*. Death domain assembly mechanism revealed by crystal structure of the oligomeric PIDDosome core complex. *Cell* **128**, 533–546 (2007).

113. Li, Y. *et al.* Cryo-EM structures of ASC and NLRC4 CARD filaments reveal a unified mechanism of nucleation and activation of caspase-1. *Proc Natl Acad Sci USA* **115**, 10845–10852 (2018).

114. López-Otín, C., Blasco, M. A., Partridge, L., Serrano, M. & Kroemer, G. Hallmarks of aging: An expanding universe. *Cell* **186**, 243–278 (2023).

115. Song, N. *et al.* NLRP3 phosphorylation is an essential priming event for inflammasome activation. *Mol. Cell* **68**, 185-197.e6 (2017).

116. Gack, M. U. *et al.* TRIM25 RING-finger E3 ubiquitin ligase is essential for RIG-I-mediated antiviral activity. *Nature* **446**, 916–920 (2007).

117. Padrick, S. B. & Rosen, M. K. Physical mechanisms of signal integration by WASP family proteins. *Annu. Rev. Biochem.* **79**, 707–735 (2010).

118. Walsh, J. G., Logue, S. E., Lüthi, A. U. & Martin, S. J. Caspase-1 promiscuity is counterbalanced by rapid inactivation of processed enzyme. *J. Biol. Chem.* **286**, 32513–32524 (2011).

119. Falahati, H. & Haji-Akbari, A. Thermodynamically driven assemblies and liquid-liquid phase separations in biology. *Soft Matter* **15**, 1135–1154 (2019).

120. Varadi, M. *et al.* AlphaFold Protein Structure Database: massively expanding the structural coverage of protein-sequence space with high-accuracy models. *Nucleic Acids Res.* **50**, D439–D444 (2022).

121. Oliinyk, O. S., Shemetov, A. A., Pletnev, S., Shcherbakova, D. M. & Verkhusha, V. V. Smallest near-infrared fluorescent protein evolved from cyanobacteriochrome as versatile tag for spectral multiplexing. *Nat. Commun.* **10**, 279 (2019).

122. Szklarczyk, D. *et al.* The STRING database in 2023: protein-protein association networks and functional enrichment analyses for any sequenced genome of interest. *Nucleic Acids Res.* **51**, D638–D646 (2023).

123. Stringer, C., Wang, T., Michaelos, M. & Pachitariu, M. Cellpose: a generalist algorithm for cellular segmentation. *Nat. Methods* **18**, 100–106 (2021).

124. Halfmann, R. & Lindquist, S. Screening for amyloid aggregation by Semi-Denaturing Detergent-Agarose Gel Electrophoresis. *J. Vis. Exp.* **17**, e838 (2008).

Figure1

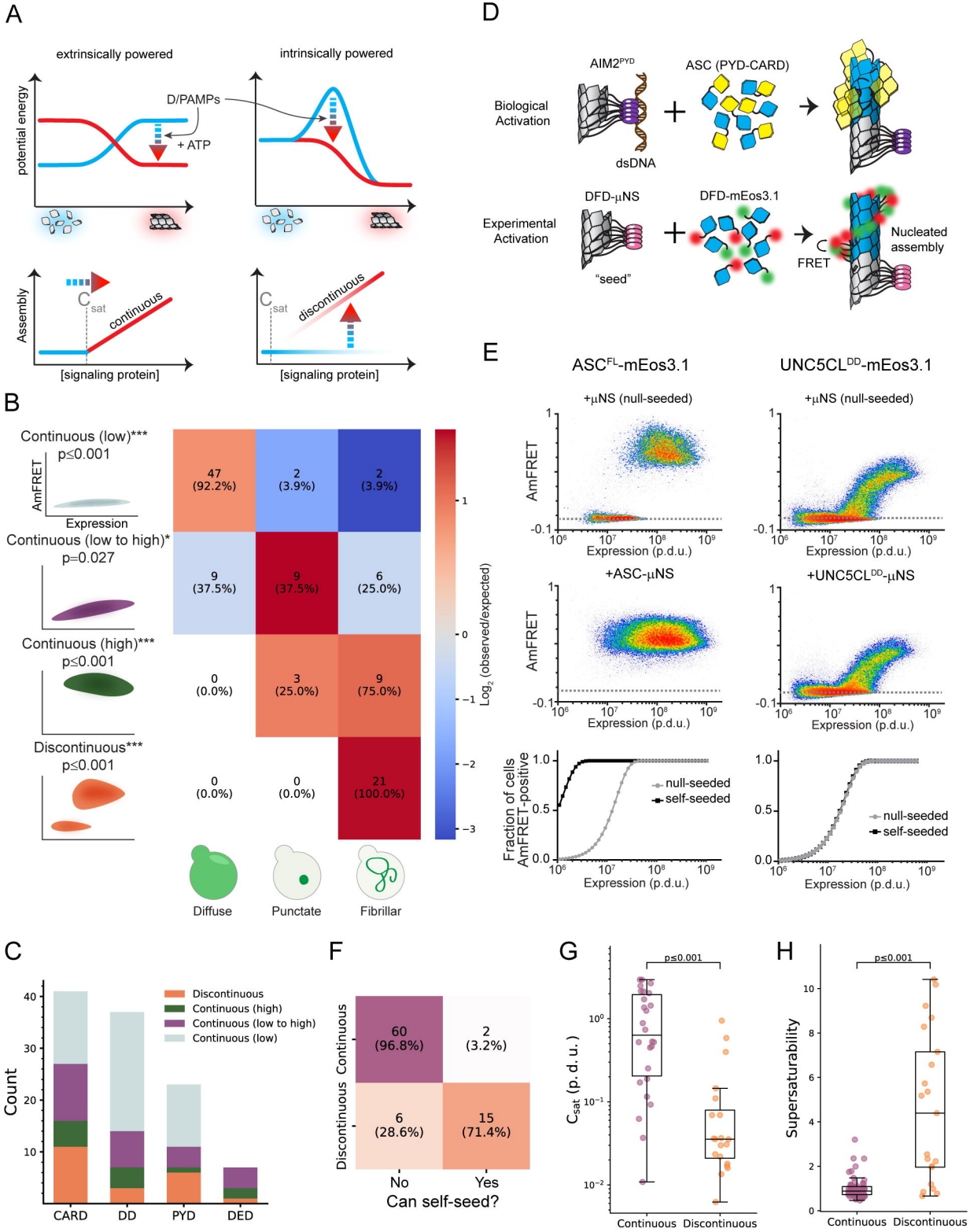
A
extrinsically powered
intrinsically powered
potential energy
D/PAMPs
+ ATP
Assembly
C sat
continuous
discontinuous
[signaling protein]
B
Continuous (low)***
p≤0.001
AmFRET
Expression
Continuous (low to high)*
p=0.027
Continuous (high)***
p≤0.001
Discontinuous***
p≤0.001
47 (92.2%)
2 (3.9%)
2 (3.9%)
9 (37.5%)
9 (37.5%)
6 (25.0%)
0 (0.0%)
3 (25.0%)
9 (75.0%)
0 (0.0%)
0 (0.0%)
21 (100.0%)
Log2 (observed/expected)
Diffuse
Punctate
Fibrillar
C
Count
Discontinuous
Continuous (high)
Continuous (low to high)
Continuous (low)
CARD
DD
PYD
DED
D
Biological Activation
AIM2PYD
dsDNA
ASC (PYD-CARD)
Experimental Activation
DFD-μNS
"seed"
DFD-mEos3.1
FRET
Nucleated assembly
E
ASCFL-mEos3.1
UNC5CLDD-mEos3.1
+μNS (null-seeded)
+ASC-μNS
+UNC5CLDD-μNS
AmFRET
Expression (p.d.u.)
Fraction of cells AmFRET-positive
null-seeded
self-seeded
F
Continuous
Discontinuous
60 (96.8%)
2 (3.2%)
6 (28.6%)
15 (71.4%)
No
Yes
Can self-seed?
G
Csat (p. d. u.)
p≤0.001
Continuous
Discontinuous
H
Supersaturability
p≤0.001
Continuous
Discontinuous

Figure 2

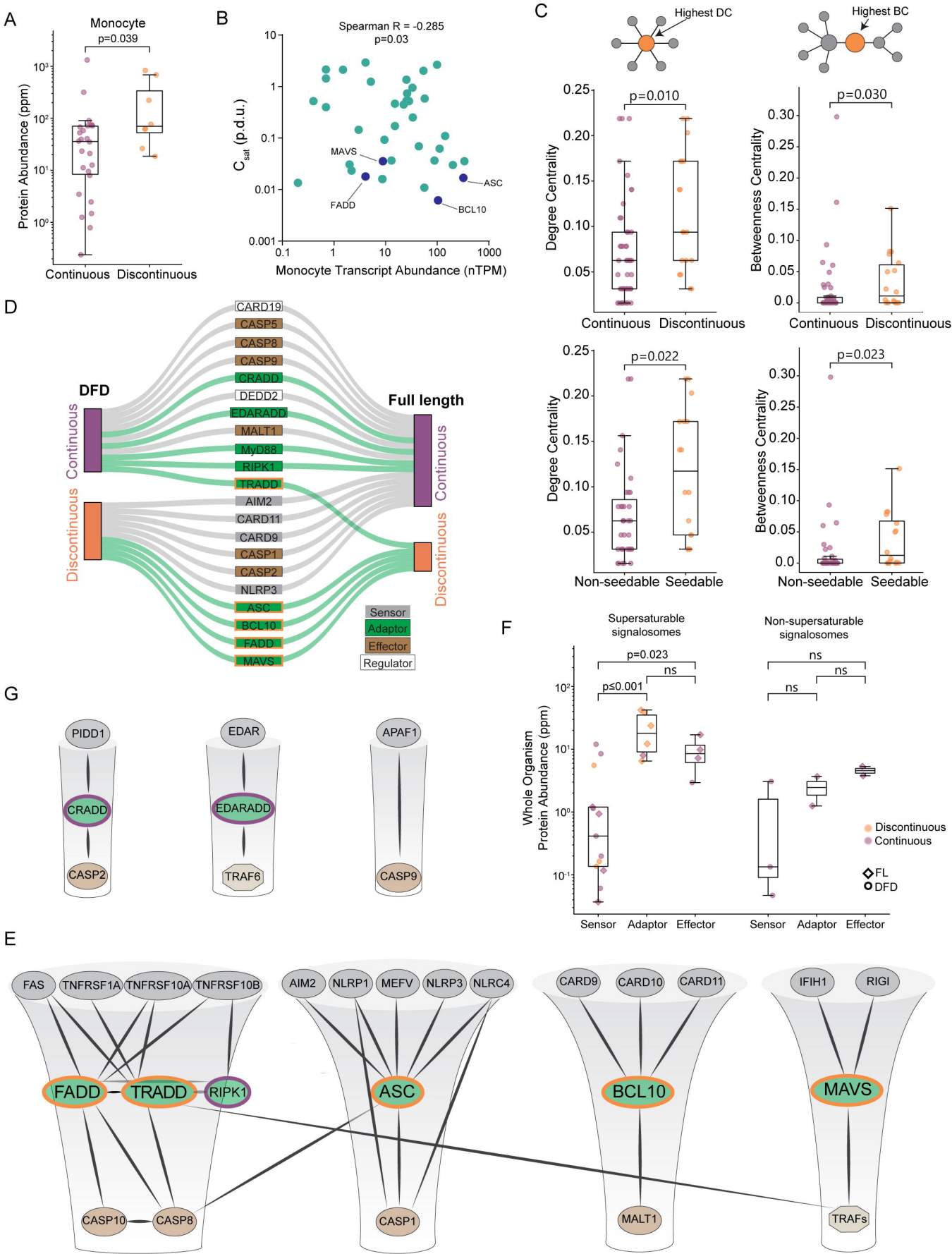
A
Monocyte
p=0.039
Protein Abundance (ppm)
Continuous
Discontinuous
B
Spearman R = -0.285
p=0.03
C_{sat} (p.d.u.)
MAVS
FADD
ASC
BCL10
Monocyte Transcript Abundance (nTPM)
C
Highest DC
Highest BC
p=0.010
p=0.030
Degree Centrality
Betweenness Centrality
Continuous
Discontinuous
p=0.022
p=0.023
Non-seedable
Seedable
D
DFD
Full length
Continuous
Discontinuous
CARD19
CASP5
CASP8
CASP9
CRADD
DEDD2
EDARADD
MALT1
MyD88
RIPK1
TRADD
AIM2
CARD11
CARD9
CASP1
CASP2
NLRP3
ASC
BCL10
FADD
MAVS
Sensor
Adaptor
Effector
Regulator
F
Supersaturable signalosomes
Non-supersaturable signalosomes
p=0.023
ns
p≤0.001
Whole Organism Protein Abundance (ppm)
Discontinuous
Continuous
FL
DFD
Sensor
Adaptor
Effector
G
PIDD1
CRADD
CASP2
EDAR
EDARADD
TRAF6
APAF1
CASP9
E
FAS
TNFRSF1A
TNFRSF10A
TNFRSF10B
AIM2
NLRP1
MEFV
NLRP3
NLRC4
CARD9
CARD10
CARD11
IFIH1
RIGI
FADD
TRADD
RIPK1
ASC
BCL10
MAVS
CASP10
CASP8
CASP1
MALT1
TRAFs

Figure 3

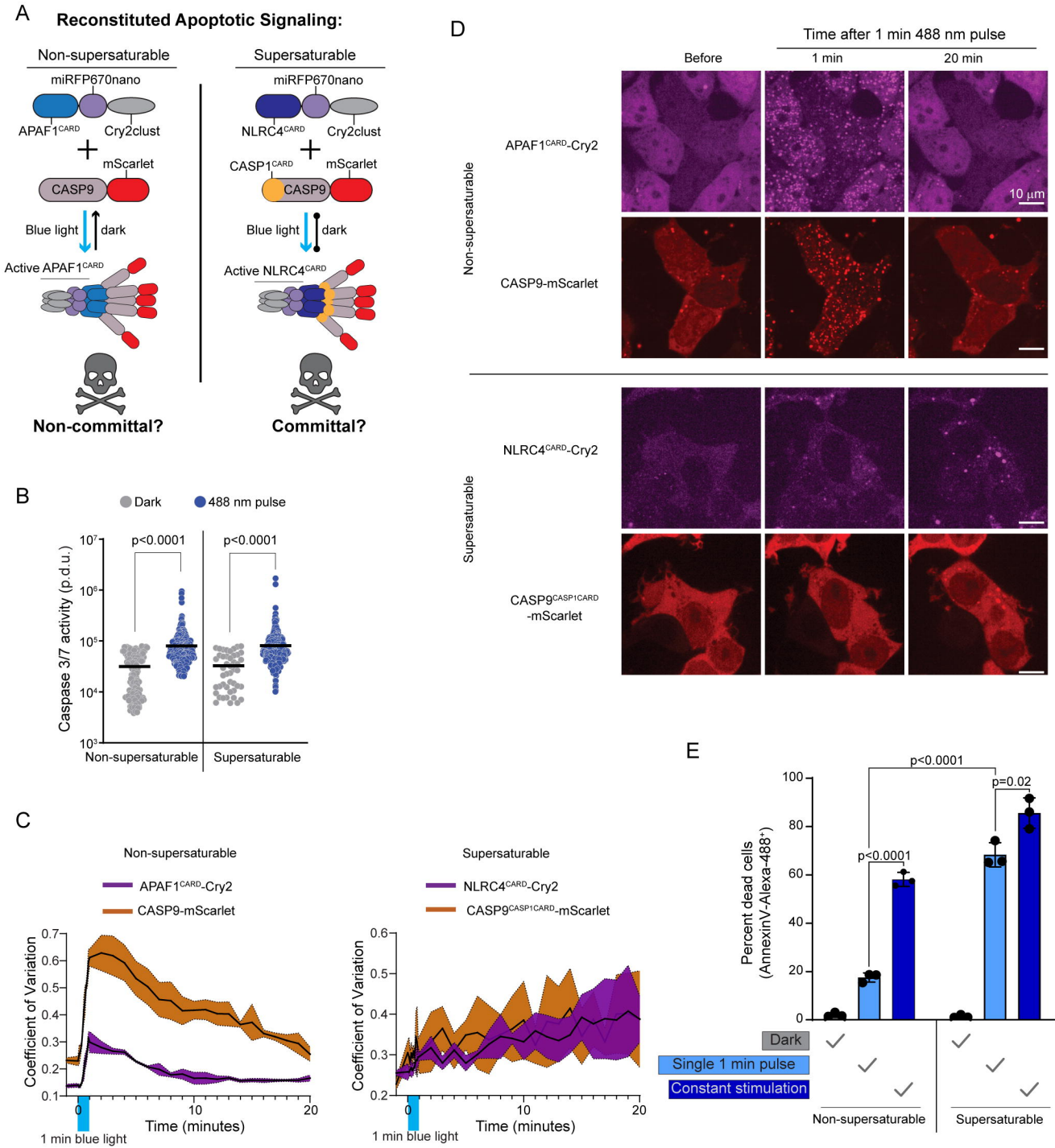
A
Reconstituted Apoptotic Signaling:
Non-supersaturable
Supersaturable
miRFP670nano
APAF1CARD
Cry2clust
mScarlet
CASP9
Blue light
dark
Active APAF1CARD
NLRC4CARD
CASP1CARD
Active NLRC4CARD
Non-committal?
Committal?
B
Dark
488 nm pulse
p<0.0001
Caspase 3/7 activity (p.d.u.)
Non-supersaturable
Supersaturable
C
Non-supersaturable
APAF1CARD-Cry2
CASP9-mScarlet
Coefficient of Variation
Time (minutes)
1 min blue light
Supersaturable
NLRC4CARD-Cry2
CASP9CASP1CARD-mScarlet
D
Time after 1 min 488 nm pulse
Before
1 min
20 min
APAF1CARD-Cry2
CASP9-mScarlet
10 µm
NLRC4CARD-Cry2
CASP9CASP1CARD
-mScarlet
E
p<0.0001
p=0.02
Percent dead cells
(AnnexinV-Alexa-488+)
Dark
Single 1 min pulse
Constant stimulation
Non-supersaturable
Supersaturable

Figure 4

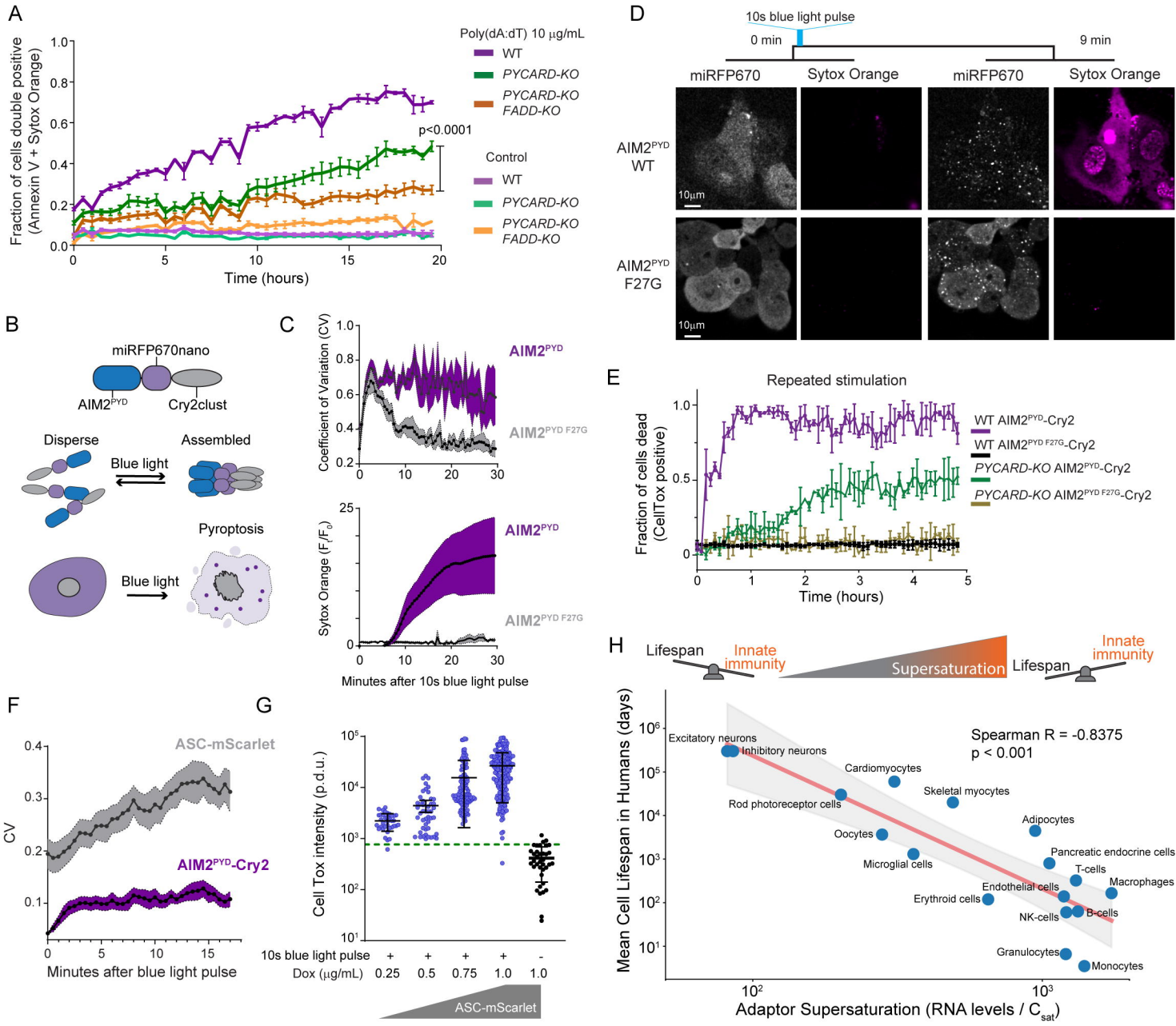
A
Fraction of cells double positive (Annexin V + Sytox Orange)
Time (hours)
Poly(dA:dT) 10 μg/mL
WT
PYCARD-KO
PYCARD-KO FADD-KO
p<0.0001
Control
WT
PYCARD-KO
PYCARD-KO FADD-KO
B
miRFP670nano
AIM2PYD
Cry2clust
Disperse
Assembled
Blue light
Pyroptosis
Blue light
C
Coefficient of Variation (CV)
AIM2PYD
AIM2PYD F27G
Sytox Orange (F/F0)
AIM2PYD
AIM2PYD F27G
Minutes after 10s blue light pulse
D
10s blue light pulse
0 min
9 min
miRFP670
Sytox Orange
miRFP670
Sytox Orange
AIM2PYD WT
AIM2PYD F27G
10μm
10μm
E
Repeated stimulation
Fraction of cells dead (CellTox positive)
WT AIM2PYD-Cry2
WT AIM2PYD F27G-Cry2
PYCARD-KO AIM2PYD-Cry2
PYCARD-KO AIM2PYD F27G-Cry2
Time (hours)
F
CV
ASC-mScarlet
AIM2PYD-Cry2
Minutes after blue light pulse
G
Cell Tox intensity (p.d.u.)
10s blue light pulse + + + + -
Dox (μg/mL) 0.25 0.5 0.75 1.0
ASC-mScarlet
H
Lifespan
Innate immunity
Supersaturation
Lifespan
Innate immunity
Mean Cell Lifespan in Humans (days)
Spearman R = -0.8375
p < 0.001
Excitatory neurons
Inhibitory neurons
Cardiomyocytes
Skeletal myocytes
Rod photoreceptor cells
Adipocytes
Oocytes
Pancreatic endocrine cells
Microglial cells
T-cells
Macrophages
Endothelial cells
Erythroid cells
NK-cells
B-cells
Granulocytes
Monocytes
Adaptor Supersaturation (RNA levels / Csat)

Figure 5

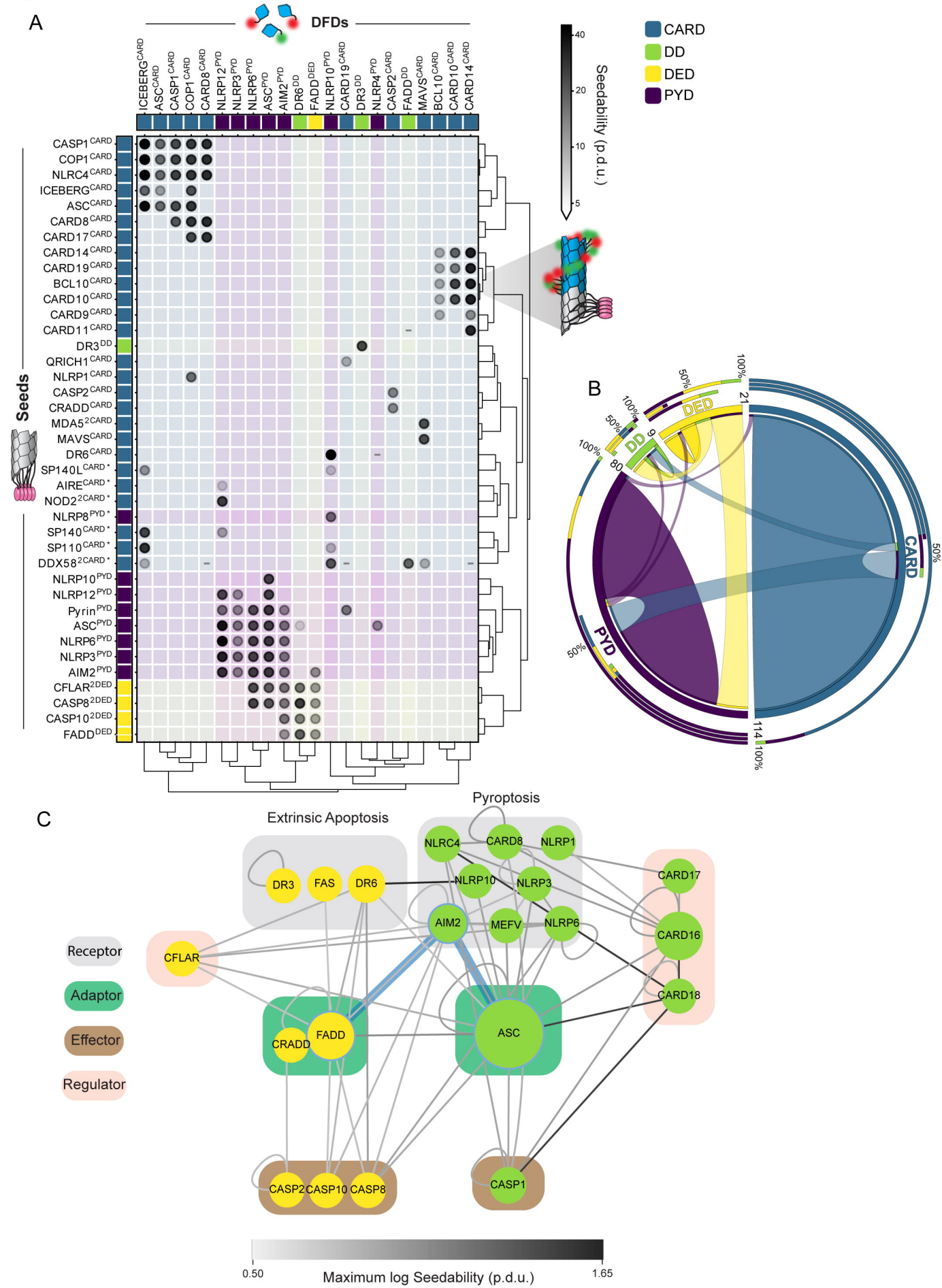
A
DFDs
Seedability (p.d.u.)
CARD
DD
DED
PYD
Seeds
B
C
Extrinsic Apoptosis
Pyroptosis
Receptor
Adaptor
Effector
Regulator
Maximum log Seedability (p.d.u.)
0.50
1.65

Figure 6

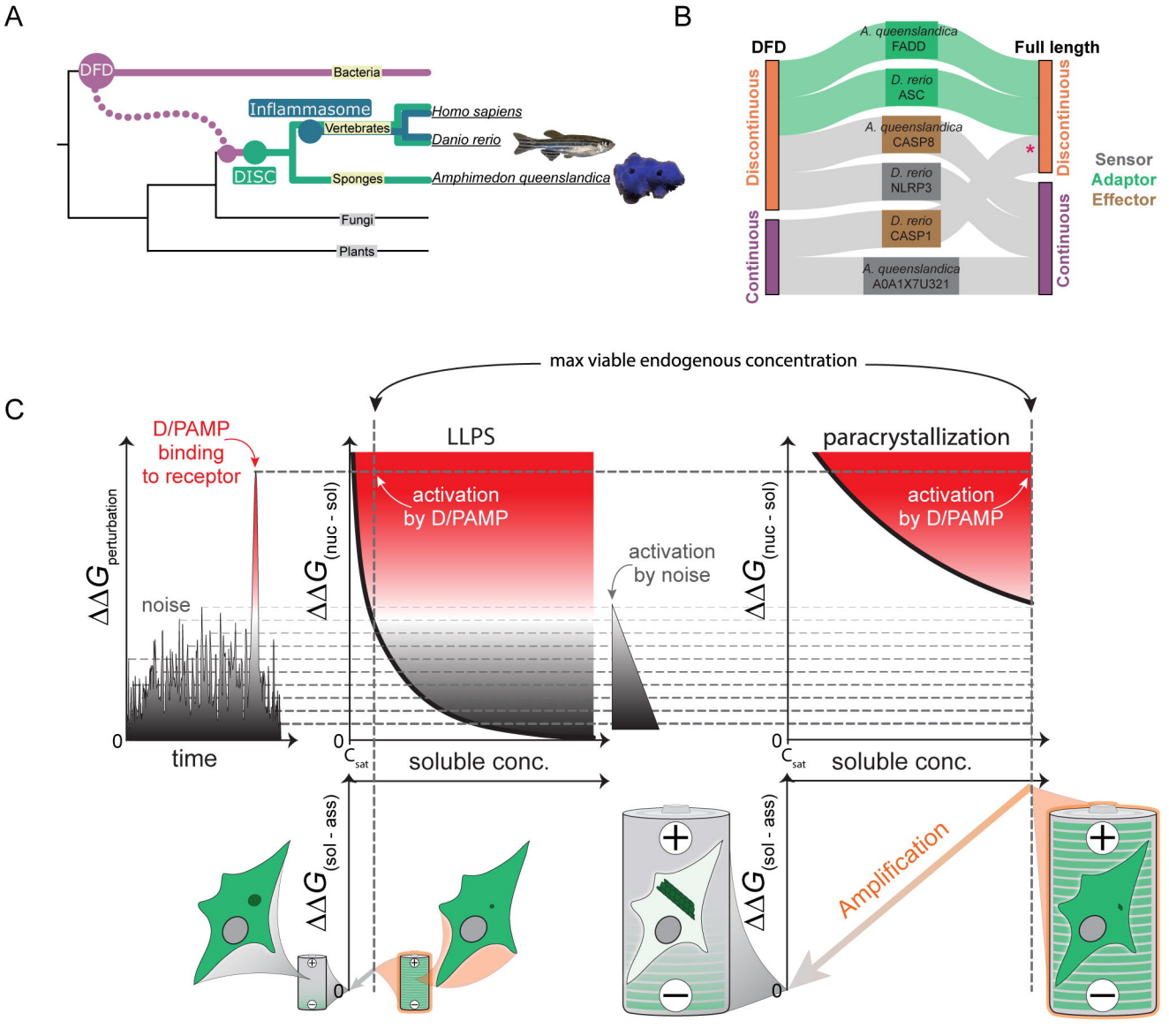
A
DFD
Bacteria
Inflammasome
Vertebrates
Homo sapiens
Danio rerio
DISC
Sponges
Amphimedon queenslandica
Fungi
Plants
B
DFD
Full length
A. queenslandica
FADD
D. rerio
ASC
A. queenslandica
CASP8
D. rerio
NLRP3
D. rerio
CASP1
A. queenslandica
A0A1X7U321
Discontinuous
Continuous
Sensor
Adaptor
Effector
C
max viable endogenous concentration
D/PAMP
binding
to receptor
noise
time
LLPS
activation
by D/PAMP
activation
by noise
paracrystallization
soluble conc.
Amplification